DEVELOPMENT AND VALIDATION OF A MATHEMATICAL MODEL FOR PREDICTING THE PERFORMANCE OF ROTARY HAMMER DRILLS

by

Will R. Didier

A Thesis Submitted in

Partial Fulfillment of the

Requirements for the Degree of

Master of Science

in Engineering

at

The University of Wisconsin-Milwaukee

May 2013

ABSTRACT
DEVELOPMENT AND VALIDATION OF A MATHEMATICAL MODEL FOR PREDICTING THE PERFORMANCE OF ROTARY HAMMER DRILLS

by

Will R. Didier

The University of Wisconsin-Milwaukee, 2013
Under the Supervision of Professor John Reisel

Rotary hammer drills are specialized drills used by plumbers, electricians, and other construction trades to drill holes in concrete. This type of tool employs a mechanism driven by an electric motor to compress a column of air, generating an impact on a drill bit to break the concrete work piece. Rotary hammer development requires the ability to accurately predict tool performance to minimize the number of prototype iterations required during the design phase and ensure the tool delivers a satisfactory level of performance. In order to predict the performance of a rotary hammer drill, a mathematical model was developed to simulate the response of the tool under load, from the time the tool is activated until it achieves steady state. Inputs for this model were taken from physical tool dimensions and motor performance data. Validation of the model was carried out by simulating the performance of a Milwaukee Electric Tool model 5262-20 rotary hammer and comparing the model outputs to actual performance data, measured following the European Power Tool Association test procedure 05/2009 – Measurement of single impact energy of rotary hammers and breakers.

TABLE OF CONTENTS

LIST OF FIGURES

LIST OF TABLES

LIST OF SYMBOLS

a_{piston}	acceleration of piston [m/s^2]
$a_{striker}$	acceleration of striker [m/s^2]
A_g	cross-section area of striker groove [m^2]
A_r	projected area of o-ring seal [m^2]
A_s	cross-section area of test rod [m^2]
$A_{striker}$	area of rear face of striker [m^2]
b_1	motor current-torque curve constant [A/N*m]
b_2	motor current-torque curve constant [A]
c_1	motor speed-torque curve constant [N*m/rpm^2]
c_2	motor speed-torque curve constant [N*m/rpm]
c_3	motor speed-torque curve constant [N*m]
C_s	speed of sound in steel [m/s]
d_{cyl}	inside diameter of piston [mm]
d_{o-ring}	inside diameter of striker o-ring [m]
$d_{striker}$	diameter of striker o-ring groove [m]

e	rebound coefficient
E	modulus of elasticity [GPa]
E_s	impact energy [J]
f_c	o-ring compression friction per length of rubbing surface [N/m]
F_c	o-ring drag due to compression [N]
F_h	o-ring drag due to pressure [N]
F_{o-ring}	o-ring drag [N]
$F_{striker}$	force acting on striker [N]
GR_1	1st stage gear ratio
GR_2	2nd stage gear ratio
I_{motor}	motor current draw [A]
J_t	rotational moment of inertia of mechanism drivetrain [kg*m^2]
k	heat capacity ratio
L	mechanism center distance [m]
L_r	length of o-ring seal rubbing surface [m]
m_{cyl}	mass of air in piston working chamber [kg]
Δm_{cyl}	change in mass of air in piston working chamber [kg]

Δm_{leak}	mass of air leakage past striker o-ring [kg]
$m_{striker}$	mass of striker [kg]
m_{piston}	mass of piston assembly [kg]
N_{motor}	motor rotational speed [rpm]
$N_{spindle}$	spindle rotational speed [rpm]
N_{is}	intermediate shaft rotational speed [rpm]
p_{atm}	atmospheric pressure [Pa]
p_{cyl}	piston working chamber air pressure [Pa]
P_{motor}	motor power output [W]
Q	striker o-ring squeeze factor
R	specific gas constant [J/kg*K]
s_d	percent stretch on striker o-ring inside diameter
S	striker o-ring percent compression
t	time [s]
Δt	time step [s]
T_a	ambient temperature [K]
T_{cyl}	piston working chamber air temperature [K}

v_{piston}	piston velocity [m/s]
$v_{striker}$	striker velocity [m/s]
Δv_{ps}	relative velocity of piston to striker [m/s]
V_{cyl}	piston working chamber volume [m^3]
w_{o-ring}	striker o-ring width [mm]
W_r	percent o-ring cross-section reduction due to stretch
x_{o-ring}	striker o-ring position
x_{piston}	piston position [m]
$x_{striker}$	striker position [m]
Δx_{ps}	relative position of piston to striker [m]
X_1	distance from wobble bearing center to rear face of piston [m]
X_2	anvil position [m]
X_6	striker length [m]
X_7	striker o-ring location [m]
X_8	striker initial position [m]
y_b	piston groove rear position [m]

y_f	piston groove front postion [m]
Y_1	distance from wobble bearing center to rear of piston groove [m]
Y_2	distance from wobble bearing center front of piston groove [m]
α_{motor}	motor angular acceleration [rad/s^2]
β	permeability rate of striker o-ring elastomer [cm^3*cm/cm^2*bar*s]
ε	strain
θ_{motor}	motor angular position [rad]
$\theta_{spindle}$	spindle angular position [rad]
θ_{is}	intermediate shaft angular position [rad]
θ_{wb}	wobble bearing race angle [rad]
θ_{wbxy}	angle between wobble bearing force vectors, X-Y plane [rad]
θ_{wbxz}	angle between wobble bearing force vectors, X-Z plane [rad]
ρ	density [kg/m^3]
τ_{bit}	torque to drive bit [N*m]
τ_{piston}	torque to drive piston assembly [N*m]
τ_{pneu}	torque to compress cylinder air column [N*m]
τ_{motor}	motor torque [N*m]

ω_{motor}	motor angular velocity [rad/s]
$\omega_{spindle}$	spindle angular velocity [rad/s]
ω_{is}	intermediate shaft angular velocity [rad/s]

ACKNOWLEDGEMENTS

The author would like to express his sincere gratitude to the individuals who made the completion of this thesis possible. Jeremy Ebner and Benjamin Ludy of the Milwaukee Electric Tool engineering staff provided invaluable input and advice during the development of this thesis and were instrumental in the formulation of the original mathematical model. The Milwaukee Electric Tool test lab staff, particularly Adam Komas and Scott Doyle, developed the experimental test fixture that made validation of the model possible and provided assistance in collecting test data. Brian Wattenbach, Troy Thorson, and Elizabeth Miller of Milwaukee Electric Tool and Dr. John Reisel of the University of Wisconsin-Milwaukee also deserve mention for facilitating the completion of this work. Finally, special thanks are given to the author's wife, Amanda Didier, for her support, understanding, and patience during the last three years.

For Mom.

1 Introduction

Rotary hammer drills are specialized power tools utilized by plumbers, electricians, and other construction trades for drilling holes in concrete or masonry. Typical applications include the drilling of pilot holes for installation of concrete fasteners or anchors and creating through holes to pass plumbing, electrical conduit, or ductwork through a wall. Additionally, when fitted with a chisel bit, rotary hammers can be used for breaking concrete or other demolition work. Rotary hammers can frequently be found in use during new construction of large high-rise buildings or warehouses, residential foundation repair, or any other construction activities involving concrete or masonry work.

Users of these tools consistently place the ability to drill holes quickly near the top of their list of needs, along with tool durability and, in the case of cordless models, the ability to complete a day's worth of work with a minimum number of recharges. In addition to meeting user needs with a new rotary hammer design, time to market is critical in gaining a competitive advantage. In order to shorten development cycles, the number of prototype iterations required to deliver the desired performance must be minimized. To achieve these goals, the rotary hammer designer must be able to accurately predict the tool's performance under various loading conditions. To that end, a mathematical model combining numerical integration techniques and FEA simulation of component impact events was developed to simulate the response of a rotary hammer from the time the tool is activated until it reaches steady state under various loading conditions. The model was then validated by simulating a tool currently

available on the commercial market and comparing the simulation result to actual tool performance data collected following an industry standard test procedure

1.1 Rotary Hammer Construction & Operation

Rotary hammers typically consist of a hammer mechanism driven by an electric motor through one or more gear reductions. The hammer mechanism consists of a reciprocating device that drives a piston. The piston compresses a column of air which in turn accelerates a metal slug, referred to as a striker, resulting in an impact with another component, the anvil. The impact generates a stress wave that travels through the anvil, along the length of the drill bit, and into the concrete work piece, causing the concrete to fracture.

The hammer mechanism, shown in Figure 1-1, begins operation as soon as the trigger switch is closed, energizing the drive motor. Torque is transmitted from the motor armature to the intermediate shaft via the first stage gear set. Mounted on the intermediate shaft is a device known as a wobble bearing, seen in Figure 1-2. The wobble bearing is a ball bearing consisting of a spherical shaft in which the bearing race is cut into the surface at an oblique angle to the axis of rotation. The outer ring of the bearing is constructed with a stem that connects to the piston via the wrist pin. The rotation of the wobble bearing shaft produces reciprocating motion at the end of the stem.

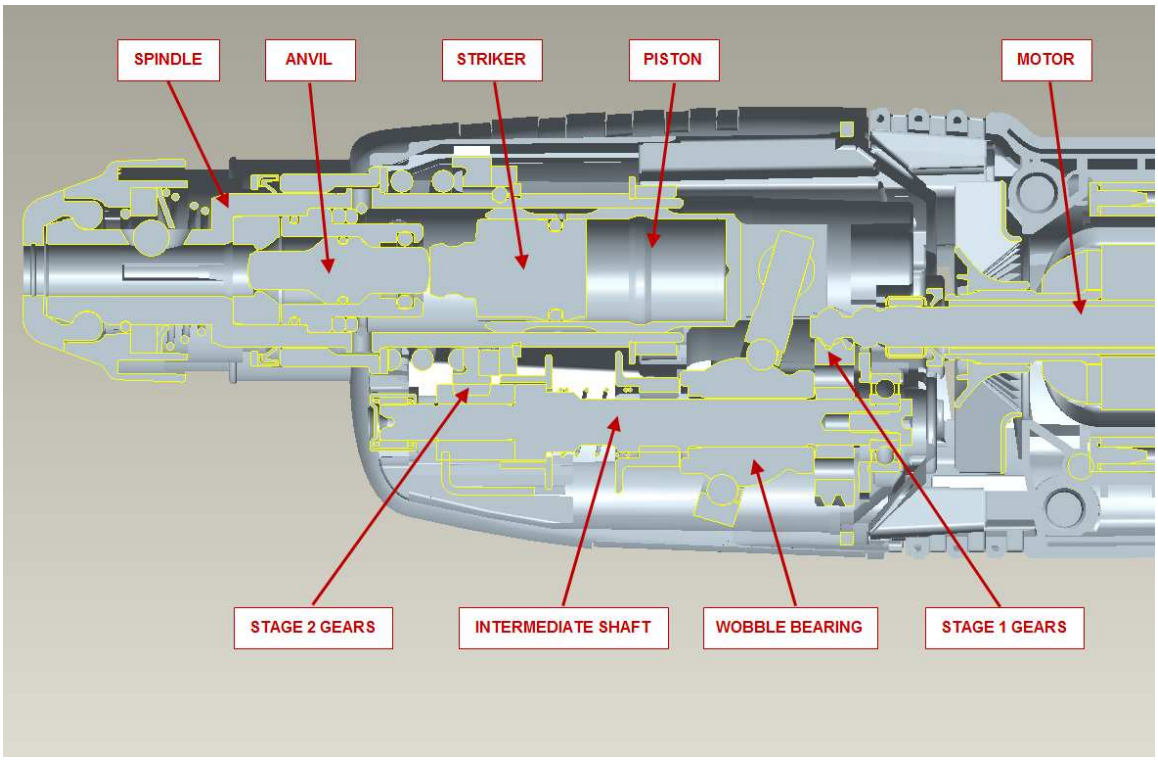

Figure 1-1 – Rotary hammer mechanism cross section

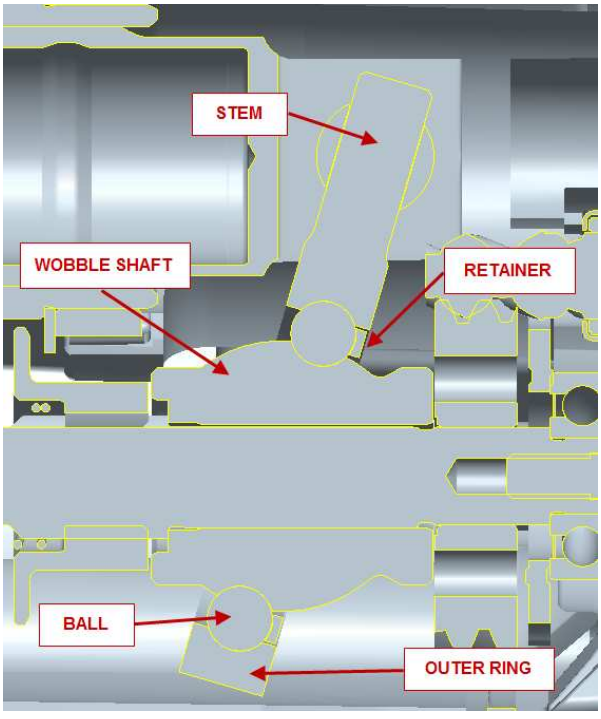

Figure 1-2 – Wobble bearing construction

The piston reciprocates in and out of the bore of the spindle, compressing the column of air trapped inside the working chamber between the piston and striker's rear faces. As the air is compressed, pressure builds inside the working chamber, propelling the striker towards the anvil, creating the energy needed to break concrete. After the impact, the piston withdraws, generating a vacuum inside the working chamber. This vacuum, along with the kinetic energy retained by the striker after impact, allows the striker to move back from the anvil with the piston, compressing the air column and beginning the next cycle. A pair of grooves, a longitudinal groove in the striker and a circumferential groove on the bore of the piston, vent the working chamber to the atmosphere during a portion of the piston's stroke. The working chamber is vented to the atmosphere any time the striker o-ring passes under the piston's groove. Air will flow in or out of the chamber by passing over the striker o-ring and down the length of the striker's groove. This vent serves to regulate the amount of pressure that can be generated inside the working chamber as well as allowing the mechanism to achieve steady state operation regardless of the initial position of the piston and striker.

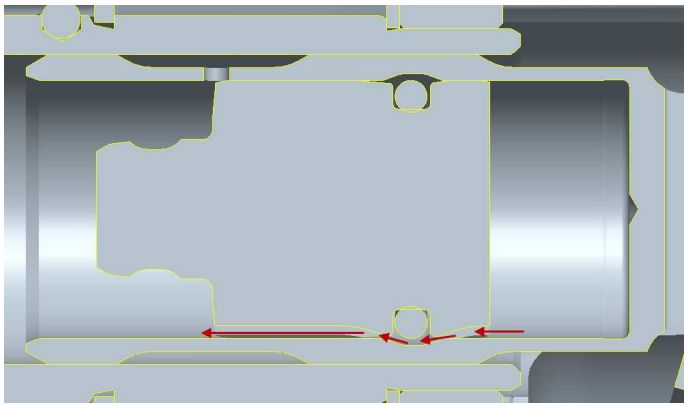

Figure 1-3 – Position of piston and striker when vent is open

Rotary hammers are typically equipped with three modes of operation: hammer-drill, drill-only, and chisel-only. These modes are controlled by a shifting mechanism that can selectively engage and disengage the wobble bearing and spindle from the torque transmitted by the intermediate shaft. One of the more common ways this is executed is by means of a pair of spring loaded couplers that engage the spindle pinion and wobble bearing. In the hammer-drill position, as shown in Figure 1-4, both couplers are locked to their respective components and the intermediate shaft transmits torque to the wobble bearing and spindle.

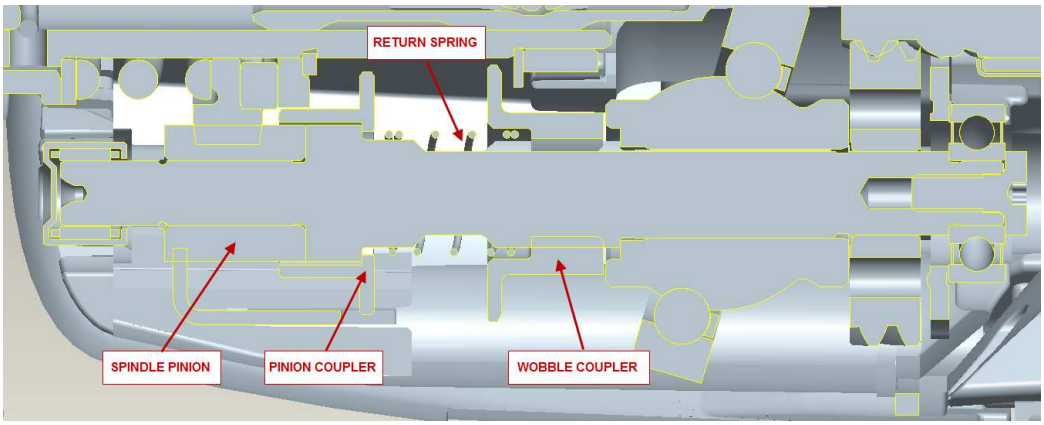

Figure 1-4 – Mechanism engaged in hammer-drill mode

When the shifting mechanism is cycled to drill only, seen in Figure 1-5, the wobble bearing coupler is retracted from the wobble bearing, disconnecting it from the drivetrain and preventing the piston and striker from generating impacts. In this mode, the tool functions as a drill and can be used to drill holes in wood, metal, or other non-masonry materials.

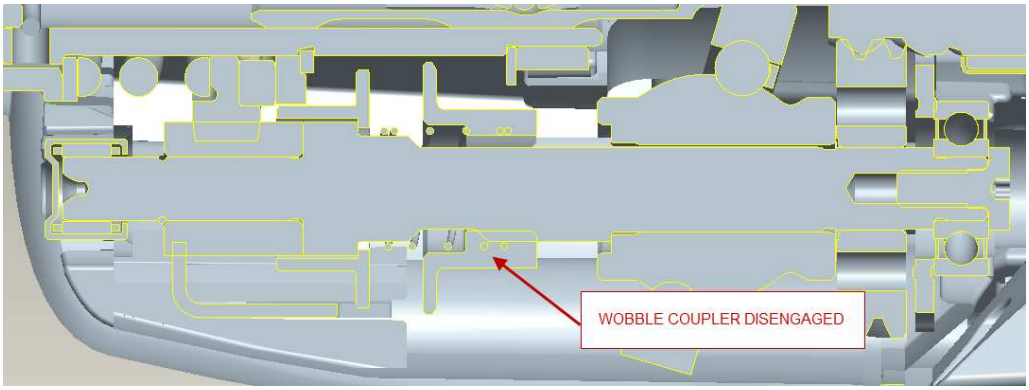

Figure 1-5 – Mechanism engaged in drill-only mode

In the chisel-only mode, depicted in Figure 1-6, the spindle pinion coupler is disengaged, preventing torque from being transmitted to the spindle. Additionally, the same linkage that retracts the coupler also engages a spindle lock on the spindle pinion, preventing the spindle from rotating. The chisel-only mode is employed in demolition work and in flash removal on newly poured concrete slabs.

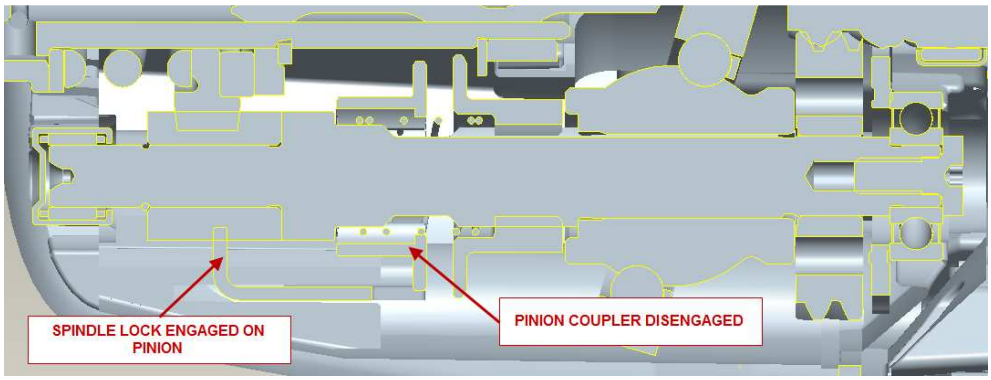

Figure 1-6 – Mechanism engaged in chisel-only mode

Rotary hammers also typically include an idling function to quickly dissipate the kinetic energy of the striker and prevent impacts from occurring when the bit is removed from the work piece. This function is necessary to prevent the tool from being

damaged by impact stress waves reflected back into the tool rather than into the concrete as intended. A common means of achieving this function is to integrate a catch barb onto the impact end of the striker. When the bit is removed from the work piece while it is still activated, the striker will impact the anvil, pushing it a short distance down the spindle. This anvil travel allows the striker to continue forward, pushing the striker barb past a catch o-ring and holding it in place against the vacuum generated in the piston working chamber during its return stroke. A vent placed in the piston wall near the leading edge allows the vacuum in the chamber to be relieved when the tool is idled. The energy of the last impact is dissipated when the anvil collides with the brake ring placed inside the spindle. To exit idle mode, the user simply presses the bit down on the work piece. This causes the connection end of the bit to travel into the spindle, pushing the anvil against the striker and disengaging the barb from the catch o-ring. Figure 1-7 shows a tool that has been placed in idle mode.

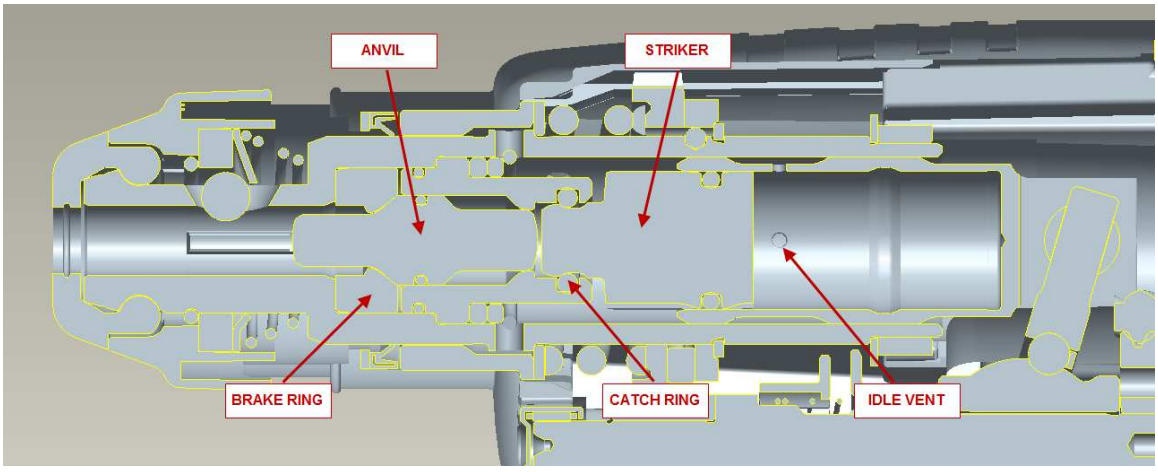

Figure 1-7 – Mechanism in idle mode

The final key component required in a rotary hammer is the bit retention system. Rotary hammers with impact energy outputs of up to 4.0J typically utilize an industry standard bit retention system known as SDS-Plus (1), (2), (3), (4). To install a bit, the user inserts a bit into the spindle, pushing against a spring-loaded retainer ball and toggle plate. The retainer ball engages a mating feature machined into the connection end of the bit, while a pair of keys on the spindle bore engage slots on the bit to transmit torque. To remove, the chuck sleeve is pulled back, compressing the spring and releasing the retainer ball. The bit can then be removed from the spindle. A typical execution of this bit retention system can be seen in Figure 1-8.

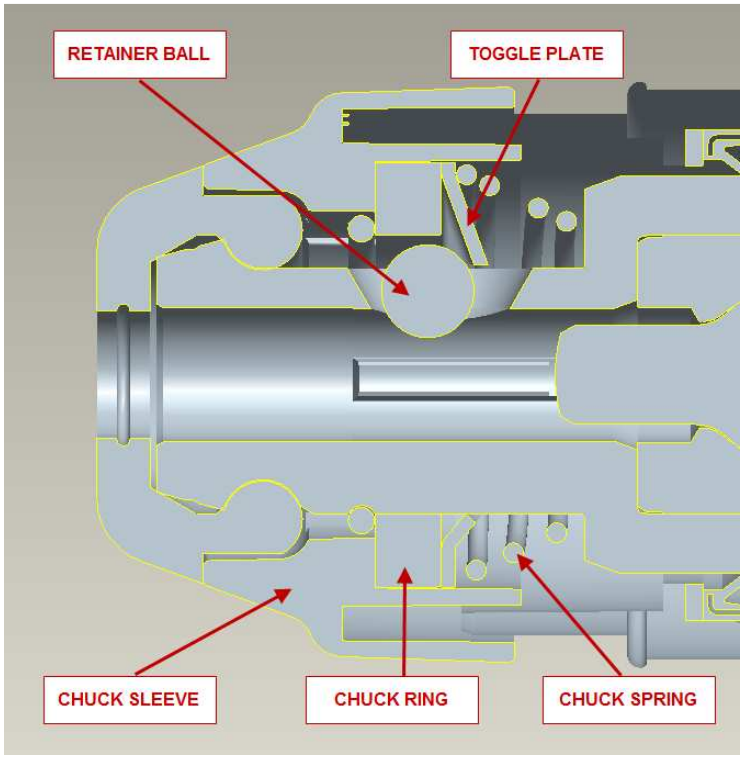

Figure 1-8 – Typical SDS-Plus bit retention system

1.2 Subject Tool

The tool chosen for study was the Milwaukee Electric Tool Corporation model 5262-60 rotary hammer, seen in Figures 1-9 and 1-10 (5). This rotary hammer is a 2kg-class hammer with a D-handle form factor and inline motor layout. The tool is driven by a 120V AC electric motor. The published specifications and performance of the tool are listed in Table 1-1 (6).

Figure 1-9 – Milwaukee Electric Tool 5262-20 rotary hammer (6)

Figure 1-10 – 5262-20 rotary hammer in a typical drilling application (6)

Specification	
Operating voltage [VAC]	120
Rated current [A]	7.0
Maximum hole size in concrete [in]	7/8
Impact energy [J]	2.44
No-load spindle speed [min^{-1}]	0-1500
No-load impact frequency [min^{-1}]	0-5625
Length [in]	17
Weight [lb]	5.8

Table 1-1: Published specficiations, 5262-20 rotary hammer

1.3 Study Objectives

The primary objective of this study is the development of a mathematical model for the prediction of the performance characteristics of rotary hammers. This model will allow the design engineer to estimate the performance of candidate rotary hammer designs before the first physical prototype is constructed. Additionally, secondary outputs calculated by the model, such as force, torque, and acceleration, can be used to inform the design of tool components and subsystems.

The completed model will be validated by inserting dimensions and specifications of the subject tool described in the previous section into the model, simulating its performance. The performance parameters calculated by the model will then be compared to the tool's actual measured performance as measured per European Power Tool Association (EPTA) test standard 05/2009 – Measurement of single impact energy of rotary hammers and breakers.

Chapter 2 details the formulation of the mathematical model that describes the kinematics of the mechanism components and thermodynamic conditions inside the piston working chamber. Chapter 3 discusses how the FEA simulation of the impact of the striker on the anvil was set up and how the results were used as an input for the model. Chapter 4 discusses the construction of the impact energy test fixture and the procedure by which impact energy data was collected.

2 Mathematical Model

In order to estimate rotary hammer performance, it was necessary to develop a mathematical model to describe the kinematics of the tool's mechanism and the thermodynamic properties of the air column inside the working chamber of the piston. The model is iterative, starting at t = 0 with the mechanism at rest, proceeding to a steady state condition representing the tool in its normal operating condition. A backward finite-difference numerical integration technique is used to calculate angular and linear positions and velocities of mechanism components at each time step (7). Other model parameters are calculated at each time step based on these positions and velocities.

2.1 Model Inputs

A number of key physical quantities and dimensions characteristic to the tool's mechanism are required as inputs for calculation of various model parameters. Figure 2-1 shows a cross section of the mechanism and highlights the specific dimensions that are used as model inputs.

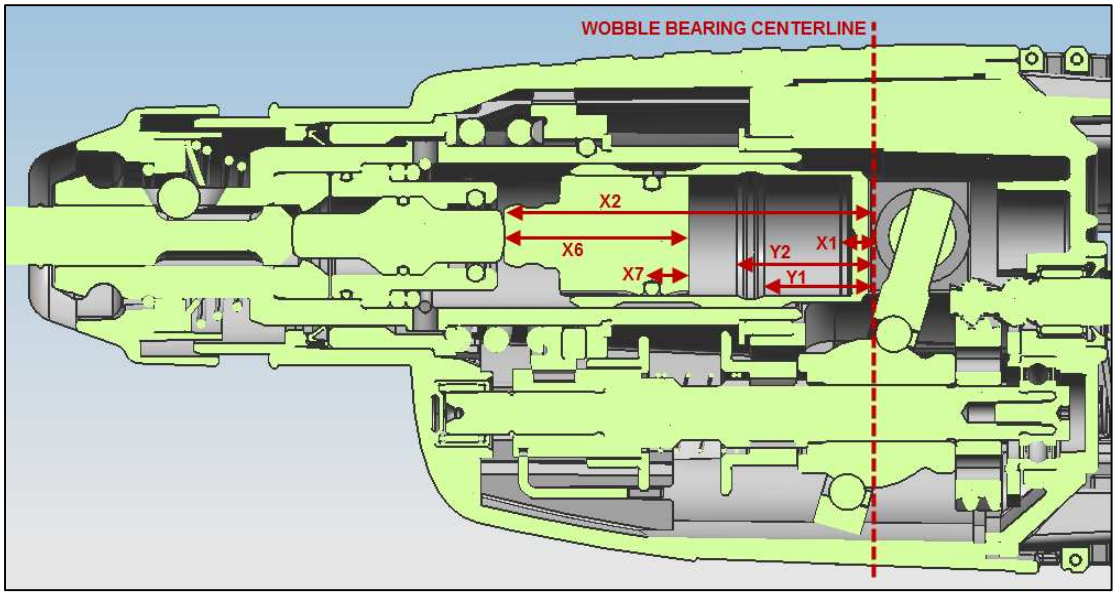

Figure 2-1: Tool mechanism cross section, 5262-20 rotary hammer

All of the length and area dimensions are nominal dimensions and were measured from a three-dimensional CAD model of the tool. Additionally, moments of inertia for rotating components on the mechanism drivetrain were derived via analysis of three-dimensional CAD data for the tool and combined into the total rotational moment of inertia, J_t, seen by the motor. Masses for the striker and piston assemblies were also taken from analysis of the tool CAD.

Certain inputs for the mathematical model were not directly measureable, namely, the constants for the motor performance curves and striker o-ring friction and leakage parameters. Generation of motor performance curve constants will be discussed in the following section. O-ring friction and leakage parameters were taken from the Parker O-Ring Handbook (8) and will covered in detail in Section 2.4.

2.2 Mechanism Kinematics

2.2.1 Motor

The model starts with the calculation of the motor's angular position and velocity. Velocity and position at each time step are determined using the Euler method (7) and are described by Equations 2-1 and 2-2, respectively.

$$\theta_{motor_n} = \theta_{motor_{n-1}} + \left(\omega_{motor_{n-1}} \Delta t\right) \qquad (2\text{-}1)$$

$$\omega_{motor_n} = \omega_{motor_{n-1}} + \left(\alpha_{motor_{n-1}} \Delta t\right) \qquad (2\text{-}2)$$

The motor's angular acceleration is given by Equation 2-3 and is a function of the torque provided by the motor, the load applied to the tool, and the rotational inertia of the mechanism drivetrain. The load on the tool is produced by three sources: the cyclic compression of air column to drive the striker, the reciprocating mass of the piston assembly, and drag on the bit as it rotates in the hole being drilled.

$$\alpha_{motor_n} = \frac{\tau_{motor_n} - \left(\frac{\tau_{pneu_n} + \tau_{piston_n}}{GR_1}\right) - \left(\frac{\tau_{bit_n}}{GR_1 GR_2}\right)}{J_t} \qquad (2\text{-}3)$$

The expression for motor torque comes from a curve fitted to actual test data of the motor's performance. This data was obtained by running a sample of four tools on a dynamometer at various load points, correcting the data for inertia and gear ratio, and averaging the results to obtain a curve of motor speed in revolutions per minute as a function of torque. Multiple tools are required to generate this data because, as a general rule, power tool motors are understood to vary as much as $\pm$10% from the

nominal designed performance due to manufacturing variances. Since the motor's speed is known at the current time step from Equation 2-2, the curve fit is rearranged to give torque in terms of speed:

$$\tau_{motor_n} = c_1 {N_{motor_n}}^2 + c_2 N_{motor_n} + c_3 \quad (2\text{-}4)$$

where c_1, c_2, and c_3 are constants from the curve fit specified in Table 2-1.

The motor's angular velocity also needs to be converted to revolutions per minute in order to be used in Equation 2-4:

$$N_{motor_n} = \frac{30\omega_{motor_n}}{\pi} \quad (2\text{-}5)$$

In addition to torque, the motor performance data plotted in Figure 2-1 is used to estimate the current draw of the tool:

$$I_{motor_n} = b_1 \tau_{motor_n} + b_2 \quad (2\text{-}6)$$

where b_1 and b_2 are constants from the curve fit specified in Table 2-1.

2.2.2 Intermediate Shaft & Spindle

With the response of the motor defined, position and velocity of the intermediate shaft and spindle can be found. In a similar fashion to the motor, angular position for the intermediate shaft and spindle are determined at each time step via the Euler method:

$$\theta_{is_n} = \theta_{ws_{n-1}} + (\omega_{ws_{n-1}} \Delta t) \quad (2\text{-}7)$$

$$\theta_{spindle_n} = \theta_{spindle_{n-1}} + \left(\omega_{spindle_{n-1}} \Delta t\right) \quad (2\text{-}8)$$

The angular velocity for the intermediate shaft is easily calculated from the motor's angular velocity and the first stage gear ratio:

$$\omega_{is_n} = \frac{\omega_{motor_n}}{GR_1} \qquad (2\text{-}9)$$

Intermediate shaft velocity and the second stage gear ratio provide the spindle angular velocity:

$$\omega_{spindle_n} = \frac{\omega_{ws_n}}{GR_2} \qquad (2\text{-}10)$$

Converting the angular velocities of the intermediate shaft and spindle to revolutions per minute provides two useful pieces of information about the tool performance; spindle speed and impacts per minute (IPM). IPM is the frequency with which the tool strikes the work piece. Equation 2-11 provides the expression for the intermediate shaft rotational speed and Equation 2-12 is the expression for the spindle rotational speed

$$N_{is_n} = \frac{30\omega_{ws_n}}{\pi} \qquad (2\text{-}11)$$

and

$$N_{spindle_n} = \frac{30\omega_{spindle_n}}{\pi} \qquad (2\text{-}12)$$

Spindle speed and IPM predicted by the model can be compared to the spindle speed measured while drilling to check that the motor performance data input into the model is accurate and the motor response is modeled correctly. Additionally, both of these quantities are typically advertised in rotary hammer marketing literature.

2.2.3 Piston

The position of the piston can be determined using the angular position of the intermediate shaft, the center distance between the intermediate shaft and the spindle, the distance from the piston's rear face to the wobble bearing centerline, and the angle of the wobble bearing raceway. With the piston position known, the piston's velocity and acceleration at each time step can then be found:

$$v_{piston_n} = \frac{x_{piston_n} - x_{piston_{n-1}}}{\Delta t} \qquad (2\text{-}14)$$

and

$$-a_{piston_n} = \frac{v_{piston_n} - v_{piston_{n-1}}}{\Delta t} \qquad (2\text{-}15)$$

Additionally, the position of the trailing and leading edges of the groove in the piston bore must be known:

$$y_{b_n} = x_{piston_n} + Y_1 - X_1 \qquad (2\text{-}16)$$

and

$$y_{f_n} = x_{piston_n} + Y_2 - X_1 \qquad (2\text{-}17)$$

The groove position will be used later in the model as a means of determining whether the working chamber of the piston is sealed or open to the atmosphere. This, combined with the position of the striker's o-ring and the difference between atmospheric and chamber pressure, indicates the flow condition of the working chamber: closed, intake, or outlet.

2.2.4 Striker

The equations that define the motion and impact force of the striker couple the kinematic behavior of the mechanism to the thermodynamic properties of the air inside the piston's working chamber. The position, velocity, and acceleration of the striker are all derived from the force acting on the striker at any given instant. This force is generated by the pressure of the air column trapped inside the piston working chamber, which is dependent on the thermodynamic conditions inside the piston.

The position of the striker at a given time step is calculated using the first three terms of a Taylor series (7):

$$x_{striker_n} = x_{striker_{n-1}} + v_{striker_{n-1}}\Delta t + \frac{1}{2}a_{striker_{n-1}}\Delta t^2 \quad (2\text{-}18)$$

The value of striker position is limited in the model such that it can never exceed the distance between the wobble bearing centerline and the point of impact with the anvil, X_2.

Striker velocity is calculated similarly to position, this time using only the first two terms of the Taylor series:

$$v_{striker_n} = \begin{cases} v_{striker_{n-1}} e & x_{striker_n} \geq X_2 \\ v_{striker_{n-1}} + a_{striker_{n-1}}\Delta t & x_{striker_n} < X_2 \end{cases} \quad (2\text{-}19)$$

As can be seen in Equation 2-19, a special condition exists when the striker's position is at the point of impact with the anvil. In this case, the velocity of the striker is calculated using the velocity just prior to impact and the rebound coefficient of the impact. For the purposes of the model, rebound coefficient is simply the ratio of the striker's velocity immediately after an impact to velocity just prior to impact:

$$e = \frac{v_{striker_n}}{v_{striker_{n-1}}} \qquad (2\text{-}20)$$

It is also important to note that since the velocity of the striker before impact is taken to be in the positive direction and velocity after impact is in the negative direction, the value of rebound coefficient will always be negative.

The acceleration of the striker is simply calculated from the force acting on the striker and its mass:

$$a_{striker_n} = \begin{cases} 0 & x_{striker_n} = X_2,\ p_{cyl_n} > p_{atm} \\ \frac{F_{striker_n}}{m_{striker}} & all\ other\ condtions \end{cases} \qquad (2\text{-}21)$$

As with velocity, a special condition exists at the point of impact. At the moment of impact, and while the air pressure in the piston working chamber is still above atmospheric, the striker's instantaneous acceleration is taken to be zero.

The force acting on the striker arises from the air pressure inside the piston working chamber pushing the striker forward toward the anvil, atmospheric pressure resisting the forward travel of the striker, and the drag of the striker o-ring as it moves along the piston bore:

$$F_{striker_n} = \begin{cases} A_{striker}\left(p_{cyl_n} - p_{atm}\right) - F_{o-ring_n} & \Delta v_{ps_n} \leq 0 \\ A_{striker}\left(p_{cyl_n} - p_{atm}\right) + F_{o-ring_n} & \Delta v_{ps_n} > 0 \end{cases} \qquad (2\text{-}22)$$

The way striker force is calculated is dependent on the velocity of the piston relative to the striker. If the relative velocity is less than or equal to zero, the piston and striker are moving away from each other and the drag from the striker o-ring opposes acts in the

assumed negative direction, which is away from the point of impact between the striker and anvil. If relative velocity is greater than zero, the piston and striker are moving toward each other and the o-ring drag acts in the positive direction, toward the anvil. The relative velocity of the piston and striker is simply the difference in instantaneous velocity of the piston and striker:

$$\Delta v_{ps_n} = v_{piston_n} - v_{striker_n} \quad (2\text{-}23)$$

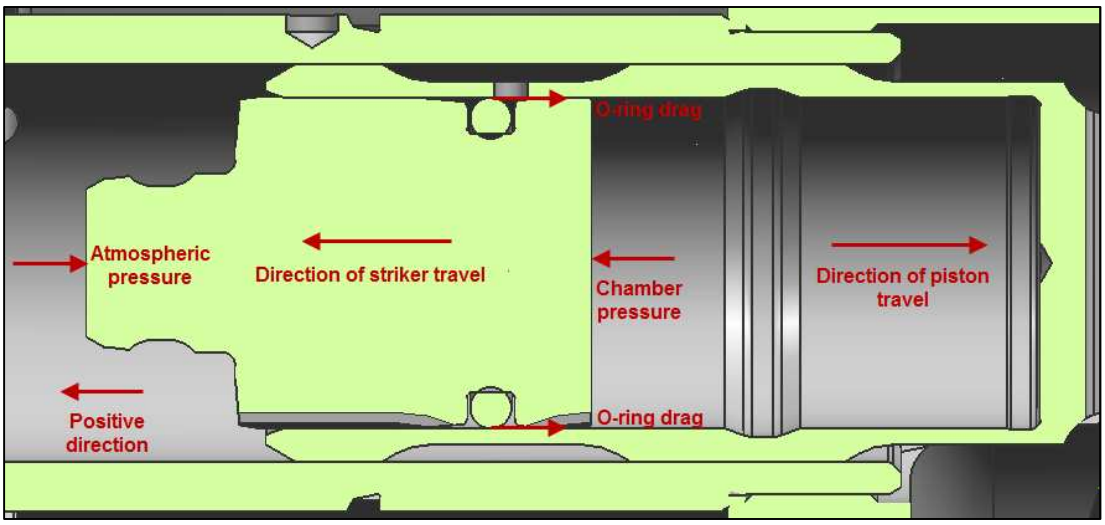

Figure 2-2: Free body diagram of forces acting on striker, $\Delta v_{ps} < 0$

There are two additional quantities associated with the striker's movement required for the model. The first is the distance between the rear faces of the piston and the striker:

$$\Delta x_{ps_n} = x_{striker_n} - X_6 - x_{piston_n} \quad (2\text{-}24)$$

This quantity is needed in order to calculate the volume of the piston working chamber at any given time step. Second is the position of the striker o-ring:

$$x_{o-ring_n} = x_{striker_n} - X_6 + X_7 \qquad (2\text{-}25)$$

2.3 Thermodynamic Properties Inside the Piston Working Chamber

2.3.1 Volume, Pressure, & Temperature

The instantaneous volume of the piston working chamber is given by:

$$V_{cyl_n} = \Delta x_{ps_n} A_{striker} \qquad (2\text{-}26)$$

Since the compression and expansion processes inside the working chamber are assumed to be adiabatic, pressure can be found using the following thermodynamic relation (9):

$$p_{cyl_n} = p_{cyl_{n-1}} \left(\frac{\rho_n}{\rho_{n-1}}\right)^k \qquad (2\text{-}27)$$

Temperature inside the working chamber is found using a form of the ideal gas law (9):

$$T_{cyl_n} = \frac{p_{cyl_n}}{\rho_n R} \qquad (2\text{-}28)$$

2.3.2 Density & Mass

The calculation for air density inside the working chamber at a given instant is dependent whether mass is able to flow in and out of the chamber. If the working chamber is sealed, the mass inside the chamber is constant, and density is simply that mass divided by the current chamber volume, as given by the first case of Equation 2-29:

$$\rho_n = \begin{cases} \frac{m_{cyl_{n-1}}}{V_{cyl_n}} & \Delta m_{cyl_n} = 0 \\ \frac{m_{cyl_{n-1}} + \Delta m_{cyl_n}}{V_{cyl_n}} & \Delta m_{cyl_n} \neq 0 \end{cases} \qquad (2\text{-}29)$$

If the chamber is open to atmosphere, however, mass is able to either enter or exit the chamber. This change in mass is taken into account in the density calculation, as can be seen in the second case of Equation 2-29.

The change in mass when the working cylinder is open to atmosphere is dependent on the pressure inside the working chamber relative to atmospheric pressure. If the pressure inside the chamber is higher than atmospheric, air will flow out of the chamber and vent to atmosphere. On the other hand, if pressure in the chamber is below atmospheric, air will flow into the chamber while it is open.

Additionally, a third case exists for air flow while the working chamber should be sealed to atmosphere. In certain instances, air is able to leak past the striker o-ring during the sealed portions of its travel inside the piston bore. This is due to the amount of compression on the o-ring in its installed condition, the pressure differential across the o-ring, and the permeability of the particular elastomer from which the o-ring is made. If the o-ring is not sufficiently compressed on assembly or if the working pressure acting on it is too great, air may be able to leak past it. The calculation of the mass change due to o-ring leakage will be expanded upon in Section 2.4.

Mass inside the working chamber at each time step is simply the product of density and volume at that time step:

$$m_{cyl_n} = \rho_n V_{cyl_n} \qquad (2\text{-}31)$$

The value of mass calculated using Equation 2-31 is subsequently used to calculate density inside the working chamber at the next time step, as seen in Equation 2-29.

2.3.3 Striker & Piston Groove

As previously discussed in Chapter 1 and Section 2.3.3, the longitudinal groove in the striker and the circumferential groove in the piston bore allow air to flow in and out of the piston working chamber during each cycle of the mechanism. This flow of air is what controls the amount of mass and air pressure inside the working chamber, ultimately affecting the amount of impact energy that the tool is able to deliver.

2.4 Striker O-Ring

In Section 2.2.4, reference was made to a drag force acting on the striker arising from friction between the striker o-ring and the piston bore. Also, the possibility for air to permeate through the o-ring, depending on the amount of compression on the o-ring and the pressure inside the piston working chamber was mentioned in Section 2.3.2. The o-ring drag force and air leakage through the o-ring are calculated using empirical formulas derived from experimental data collected by the o-ring manufacturer (8). Several parameters used in the calculation of drag force and leakage are specific to the o-ring and are published in the manufacturer's literature (8).

2.4.1 O-Ring Drag

The drag force generated by the striker o-ring as it moves along the piston's surface is made up of two components. The first comes from the compression of the o-ring when it has been installed on the striker and inserted into the piston. The second component is generated by air pressure from inside the piston working chamber and atmosphere acting on the o-ring during the piston's stroke.

The determination of the compression component begins with a calculation of the percentage of stretch on the o-ring's inside diameter after is it placed on the striker (8):

$$s_d = \left(\frac{d_{striker} - d_{o-ring}}{d_{o-ring}}\right) * 100 \qquad (2\text{-}37)$$

Next, the percent stretch on the o-ring inside diameter is used to calculate the amount of cross section reduction. The formulation for percent cross-section reduction is dependent on the amount of stretch on the inside diameter, as shown in Equation 2-37 (8):

$$W_r = \begin{cases} 0 & s_d = 0 \\ -0.005 + 1.19s_d - 0.19{s_d}^2 - 0.001{s_d}^3 + 0.008{s_d}^4 & 0 < s_d \leq 3 \\ 0.56 + 0.59s_d - 0.0046{s_d}^2 & 3 < s_d \end{cases} \qquad (2\text{-}38)$$

Then, o-ring percent compression can be calculated (8):

$$S = \left[\frac{\left(w_{o-ring} - \frac{W_r}{100 * w_{o-ring}}\right) - \left(\frac{d_{cyl} - d_{striker}}{2}\right)}{\left(w_{o-ring} - \frac{W_r}{100 * w_{o-ring}}\right)}\right] * 100 \qquad (2\text{-}39)$$

The percent compression of the o-ring is used to find the compression friction factor, f_c, as shown by Figure 2-4.

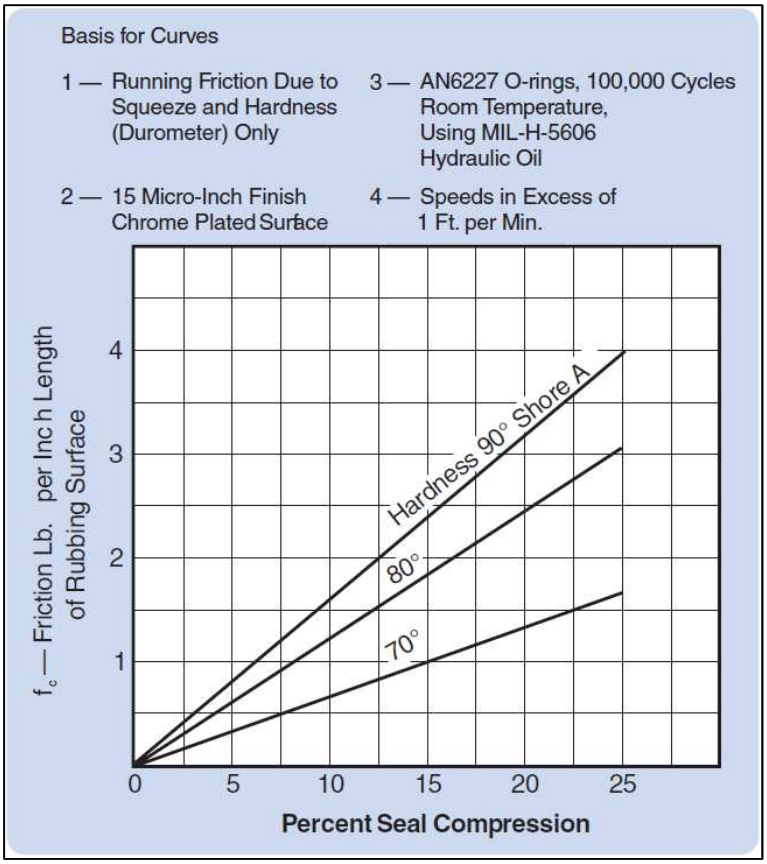

Figure 2-3: O-ring friction as a function of compression, taken from the Parker O-Ring Handbook (8)

Finally, the compression friction factor is simply multiplied by the length of the o-ring seal rubbing surface to arrive at a value for the compression-generated drag (8):

$$F_c = f_c L_r \qquad (2\text{-}40)$$

The pressure-generated portion of o-ring drag is given by the experimentally-derived plot shown in Figure 2-5. Here, drag is measured in terms of force per unit of o-ring seal projected area.

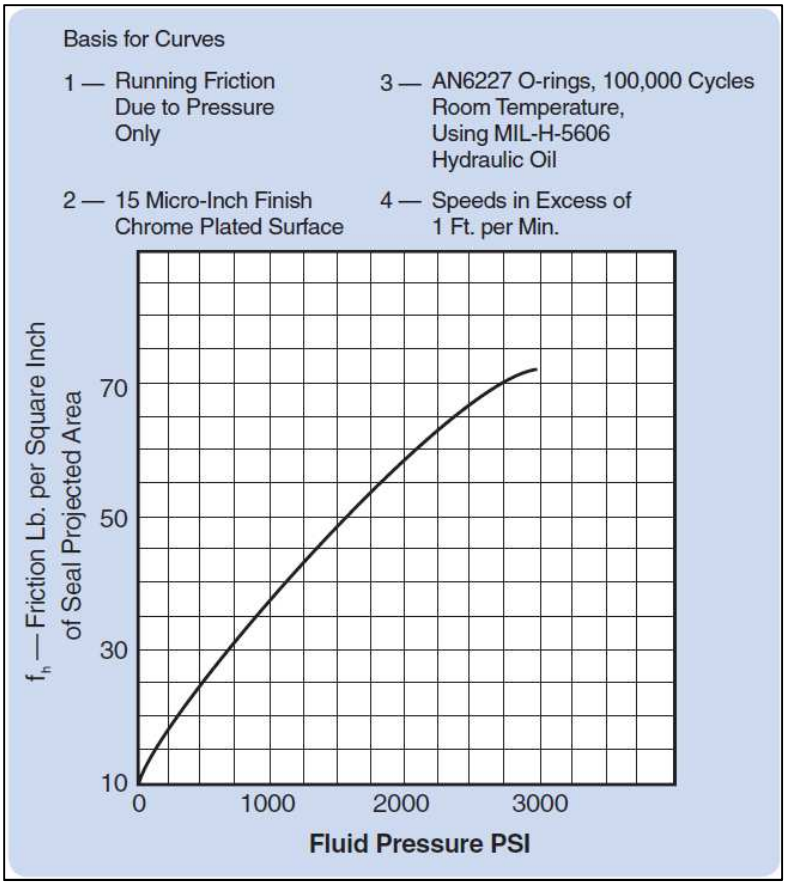

Figure 2-4: O-ring friction as a function of pressure, taken from the Parker O-Ring Handbook (8)

The pressure and compression components are summed to give the total o-ring drag at each time step:

$$F_{o-ring_n} = F_{h_n} + F_c \qquad (2\text{-}42)$$

2.4.2 O-Ring Leakage

There exists the possibility for air to escape from the piston working chamber by permeating through the o-ring elastomer. The amount of air that is able to escape is dependent on the permeability of the elastomer, the compression on the o-ring in assembled condition, and the pressure differential across the seal. Equation 2-43 is a modified version of an equation recommended by the Parker O-Ring Handbook (8) for the estimation of leak rate through an o-ring seal. In order to suit the purposes of the model, the time step and density of air at the piston vent are appended to the equation to convert leak rate to the actual mass of air leaking past the seal at each time step. Also, conversion factors are applied to o-ring inside diameter, pressure, and density to ensure consistent units (8).

$$\Delta m_{leak_n} = \beta \frac{d_{o-ring}}{10}\left[1 \times 10^{-5}\left(p_{atm} - p_{cyl_n}\right)\right] Q \left[1 - \frac{S}{100}\right]^2 \Delta t \frac{\rho_{exit_n}}{1000000} \qquad (2\text{-}43)$$

In addition to pressure and o-ring compression, two other factors are introduced. The first is the permeability factor, β, of the o-ring elastomer. The second factor is the o-ring squeeze factor, which is a function of o-ring percent squeeze, given by the following equation (8):

$$Q = -51.282S^5 + 80.42S^4 - 36.026S^3 + 5.9435S^2 - 0.3112S + 0.7512 \qquad (2\text{-}44)$$

2.5 Loads Applied to Tool

2.5.1 Pneumatic & Reciprocating Mass Loads

The first two loads applied to the tool are the torque required to generate air pressure inside the piston working chamber and accelerate the striker into the anvil and the torque required to drive the reciprocating mass of the piston assembly.

The torque supplied to these two loads is transferred to from the motor to the mechanism via the wobble bearing. The wobble bearing converts the rotational motion of the intermediate shaft into reciprocating motion, much like a crankshaft and connecting rod. The path through which the torque is transferred is complex due to the nature of the wobble bearing's motion. As such, a detailed analysis of the wobble bearing mechanics is required to develop an equation to calculate the torque supplied by the motor to the pneumatic and reciprocating mass loads.

The forces acting on the striker and the wobble bearing in the X-Z plane (vertical through centerline of tool) and the X-Y plane (horizontal through spindle axis) are shown in Figures 2-6 and 2-7, respectively.

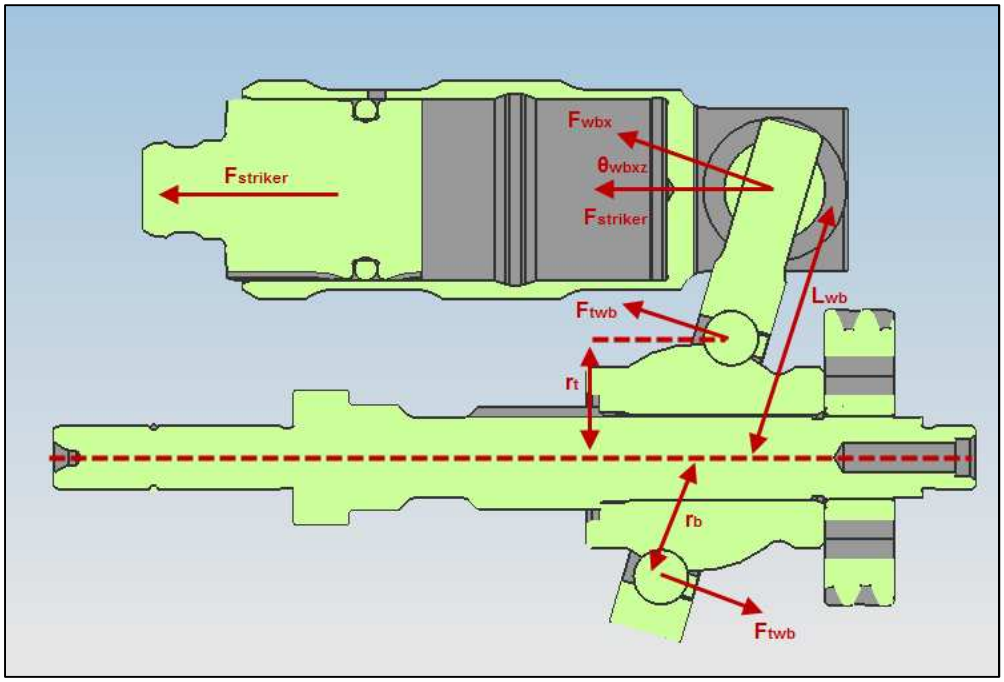

Figure 2-5: Striker and wobble bearing forces, X-Z plane

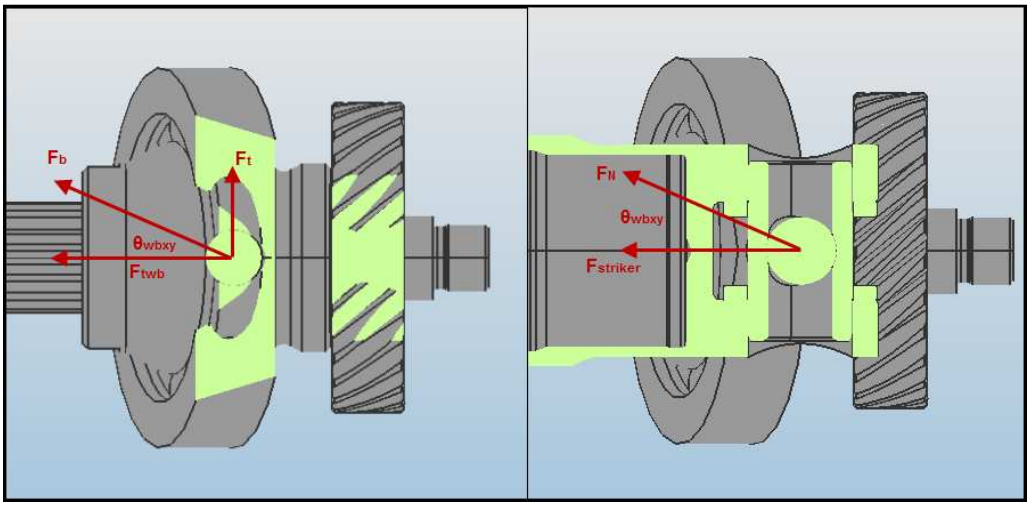

Figure 2-6: Wobble bearing forces (left) and striker forces (right), X-Y plane

In order to calculate the torque transmitted through the wobble bearing, the angle between the force applied to the striker to generate impact energy and the force

applied to the piston by the wobble bearing stem must be determined at each time step in terms of the angular position of the intermediate shaft driving the wobble bearing. The force acting on the striker is a component of the normal force, F_N, acting in the X-Y plane at the centerline of the wrist pin. F_N is in turn a component of the force acting perpendicular to the wobble stem through the wrist pin centerline, F_{wbx}. The moment arm, L_{wb}, on which F_{wbx} acts, is a function of the mechanism center distance and the angular position of the intermediate shaft. The torque acting about the wobble bearing axis normal to the X-Z plane is the same at all points along the wobble stem. The moment arm r_T corresponding to F_T is dependent on the intermediate shaft angular position and can be found using the radius of the wobble bearing. Finally, the torque about the intermediate shaft axis to drive the pneumatic load is given by the product of F_T and r_T.

The calculation of the torque to drive the piston assembly reciprocating mass is nearly identical to pneumatic torque, by simply replacing the striker force with the mass and acceleration of the piston assembly.

2.5.2 Drill Bit Drag

The final source of load comes from the drag on the drill bit as it progresses deeper into the concrete. This loading is dependent on many factors, including the size and condition of the bit, as well as the amount of force the operator applies to the tool and material properties of the work piece. Adding in the drag produced by the drill bit

provides a convenient means by which to apply load to the tool and examine the performance at various load points. At present, a reliable means of estimating or measuring drill bit drag for use in the model has not been found. However, the procedure for measuring the tool's impact energy calls for operating the tool in hammer-only mode and does not involve drilling a hole in concrete, thus the drill bit drag load will not be considered.

2.6 Model Outputs

The primary output of the mathematical model is the tool's impact energy. The impact energy is calculated by first performing a search of the model's calculated data for the time steps at which impacts occur. After an impact is found, the striker's velocity at that time step is multiplied by the rebound coefficient to give the velocity of the striker just prior to impact. This velocity, together with the striker's mass and rebound coefficient, is used to calculate the amount of the striker's kinetic energy that is transferred to the anvil. The impact energy is given by Equation 2-47:

$$E_s = \frac{1}{2} m_{striker} {v_{striker}}_{n-1}^{\,2} (1 - e^2) \qquad (2\text{-}59)$$

The impact energy of the tool is taken as the average of the energy of the last ten impacts calculated in the model, after steady state has been reached.

In addition to the tool's impact energy, several other parameters are used to gauge the tool's performance. These parameters are shown in Table 2-3. Like impact

energy, velocity, pressure, and temperature are calculated as the average of these values at the last ten calculated impacts. Impacts per minute, spindle speed, and current draw are a total average of these values at every time step during the period of time in which the last ten impacts occur.

Output	Symbol	Value	Unit
Steady state impact energy	E_s	2.34	J
Steady state current draw	I_{motor}	5.78	A
Steady state impacts per minute (IPM)	N_{is}	4372	min-1
Steady state spindle speed (RPM)	$N_{spindle}$	1166	min-1
Steady state maximum pressure	p_{cyl}	25.94	Bar
Steady state maximum temperature	T_{cyl}	740	K
Steady state striker impact velocity	$v_{striker}$	9.26	m/s

Table 2-1: Mathematical model outputs, 5262-20 rotary hammer

3 Impact Energy Testing

The previous chapters described the formulation of a mathematical model to describe rotary hammer performance, using an existing tool to demonstrate the operation of the model. In order to validate the model's accuracy, samples of the modeled tool were tested following the European Power Tool Association (EPTA) test procedure 05/2009 – Measurement of single impact energy of rotary hammers and breakers (10). The two primary performance metrics recorded by this test are the average energy delivered to the test rod with each impact and the frequency at which impacts occur.

3.1 Test Fixture

Impact energy was measured using a test fixture developed in parallel to the mathematical model by the Milwaukee Electric Tool test lab (11). The fixture was designed according to the specifications prescribed by EPTA 05/2009 (10). A schematic of the fixture can be seen in Figure 4-1.

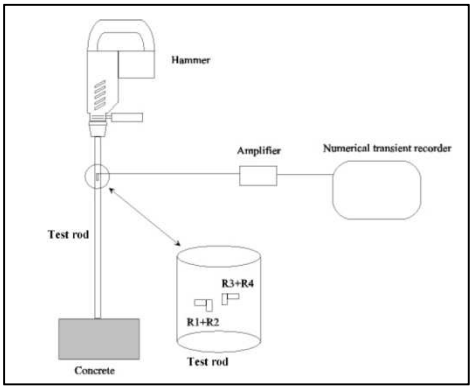

Figure 3-1: Impact energy test fixture schematic, from EPTA 05/2009 (10)

The test fixture consists of four primary elements: the test rod, the strain gauge amplifier, the data acquisition system (DAQ), and the test concrete. Additionally, a holding fixture for the test rod, a verification device, and a frame on which to mount them and position them over the concrete block were constructed.

The test rod is a bar of AISI 8630 steel 10mm in diameter, with features machined into the connection end of the rod that allow it to be installed into rotary hammers equipped with a SDS-Plus type bit retention device. The opposite end of the rod is domed with radius of 100mm to provide a consistent contact point with the concrete block.

Four strain gauges in a Wheatstone full-bridge configuration were affixed to the surface of the rod at a distance of 150mm from the connection end. This position allows the strain gauges to accurately measure the first compression stress wave from each impact of the tool without interference from tension stress waves generated by the previous impact that are reflected from the contact end of the test rod. The strain gauges were applied to the rod in pairs. Each strain gauge in the pair were oriented 90^{o} relative to each other, while the pairs were located 180^{o} apart on the surface of the test rod in order to minimize the effects of temperature, bending, or torsion of the test rod (10). The gauge output leads were soldered to a connection header for connection to the strain gauge amplifier.

The strain gauge amplifier was used to supply excitation voltage to the strain gauge bridge circuit as well as filter signal noise and condition the output signal from the

circuit. The amplifier was also used to zero out the signal generated by the application of a weighted fixture to the tool handle before the start of the test.

The DAQ system consisted of two analog input modules mounted to an I/O chassis. The first input module has the ability to capture data at a 1MHz sampling rate and was utilized to acquire the strain gauge output signal via the strain gauge amplifier. The second module samples at 250kHz and was used to capture the output signal from the verification device. The DAQ system was linked to a Hewlett-Packard 8540w laptop running LabView.

The verification device consisted of a barrel positioned below a pneumatic cylinder used to fire a metal slug at the end of a test rod.

Two lengthwise slots were cut into the barrel 180^{o} apart from each other just above the test rod, through which a laser curtain was passed. The curtain was used to measure the displacement of the metal slug before and after impacting the test rod. The displacement measurements were in turn used to calculate the slug's velocity prior to and after impact. The slug velocities were then used to calculate the quantity of the slug's kinetic energy that was transferred into the test rod using Equation 2-59:

$$E_s = \frac{1}{2} m_{striker} {v_{striker}}_{n-1}{}^2 (1 - e^2) \qquad (2\text{-}59)$$

A LabView program was developed to receive data from both the test rod strain gauges and the verification device and use it to calculate impact energy and frequency and, in the case of the verification device, the verification slug's transferred kinetic energy. The program contains an algorithm to search the strain gauge data for the first

compression stress wave of an impact and the subsequent reflected tension wave, as shown in Figure 4-4. Once this segment of data was located, the energy for the impact was calculated by evaluating Equation 4-1 over the time period between the first compression wave and the first tension wave (10).

$$E_s = A_s C_s E \int_0^T \varepsilon^2 dt \qquad (4\text{-}1)$$

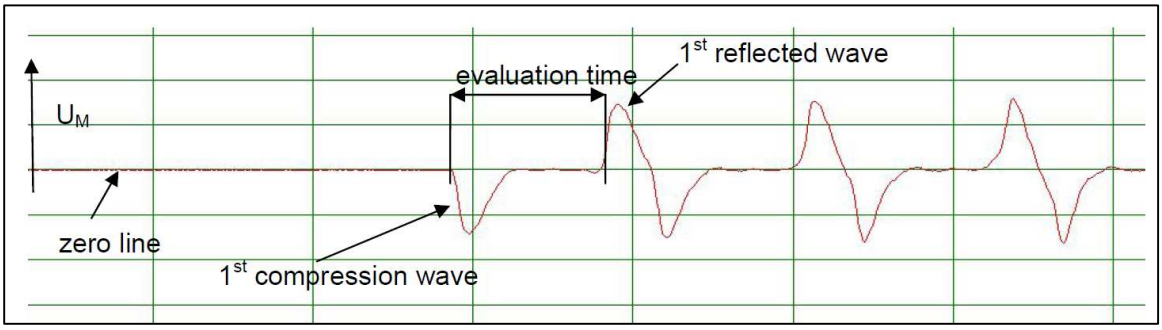

Figure 3-2: First compression wave segment used for energy calculation (10)

This search and calculation is repeated for every impact captured during the test run. The reported impact energy value for the test run is calculated as the average of the values for each individual impact. The impact frequency is simply calculated as the number of impacts captured divided by the capture time.

3.2 Test Rod Verification Procedure & Results

Prior to taking the impact energy measurements, the ability of the test rods to accurately record impact energy was verified. The test rod was inserted into the rod holder and the verification device was aligned directly over the rod to ensure that the verification slug would impact the rod straight and on center. The slug was then loaded

into the barrel of the verification device and launched toward the test rod by the pneumatic cylinder. The DAQ system simultaneously recorded the displacement signal from the laser curtain and the strain signal from the test rod. Each of these signals was used to calculate a value for energy. The kinetic energy lost to the test rod by the slug was calculated from the displacement data using Equation 2-59 while strain energy in the test rod was calculated from the strain gauge data using Equation 4-1. The two values were then compared to determine if the values for kinetic and strain energy were in agreement. The verification process was repeated five times for each rod used and the percent difference between kinetic and strain energy was computed as the average of the difference for each run. Per EPTA 05/2009, the allowable difference between measured kinetic and strain energy is 5% (10). A negative value indicates that the measured strain energy was less than the kinetic energy reported by the verification device. The results of verification testing for the test rods used in this investigation are listed in Table 4-1. Detailed results can be found in Appendix B.

Test Rod ID	% Difference of Energy Measurements
HK52	-3.04%
HK55	0.3%

Table 3-1: Test rod verification results

3.3 Impact Energy Test Procedure & Results

A sample of seven Milwaukee Electric Tool model 5262-20 rotary hammers was used to conduct impact energy testing. The sample was comprised of four new tools

drawn from factory stock and three tools returned under warranty, but classified as having no defect. This was done to minimize the number of tools used for testing that were built during the same production run and mitigate the effect of manufacturing variance on the test data.

Prior to starting each test run, the tools were warmed up by drilling ten 6” deep holes in 5000psi compressive strength concrete using a ½” carbide masonry drill bit. The warm up procedure is necessary to distribute and heat the lubricating grease inside the gears, bearings, and piston, reducing viscous friction from the grease and resulting in a consistent impact energy measurement. If the tool is not warmed up properly, this will manifest as increasing impact energy during the test run as the tool continues to warm up.

After the warm up was completed, the tool’s hammer-only mode was engaged and the tool was connected to the test rod and a 120N weight was placed over the tool handle. The weight replaces the force applied to the tool by a user and aids in keeping the anvil, test rod, and concrete in contact during the test run, minimizing the possibility for any rebound impacts that would affect the data measurement. Additionally, a grounding lead was connected to the test rod to help reduce electrical interference and noise that would affect the strain data transmitted to the amplifier. Just prior to starting the test run, the strain gauge amplifier was balanced to zero out the voltage signal produced by the strain gauges when the weight fixture was applied to the tool handle.

The next step in the test procedure was to take the actual impact energy measurement. The tool was activated and allowed to come to full operating speed, after which the data collection program was started. The program collected voltage data from the strain gauges for a period of three seconds and performed the calculations, as detailed in the previous section, to produce the measurements for average impact energy and impact frequency during the test run.

A report for each test run was automatically generated for each test run, detailing not only average impact energy and frequency, but also the energy and time for each impact and the strain signature of each impact. The additional information for each impact was used to determine if there were any irregularities in the test data that would warrant repeating the test run. A typical test run report can be seen in Figure 4-6.

A successful test run is indicated by consistent energy and duration for each impact and similarly shaped strain signatures. An impact energy plot that shows increasing energy during the test run indicates an improperly warmed up tool. A discontinuity in the time step plot or abnormally shaped strain signatures are symptoms of either insufficient force applied to the tool to prevent rebound impacts or an error in the data collection. Figure 4-7 shows an example of a test run report with errors.

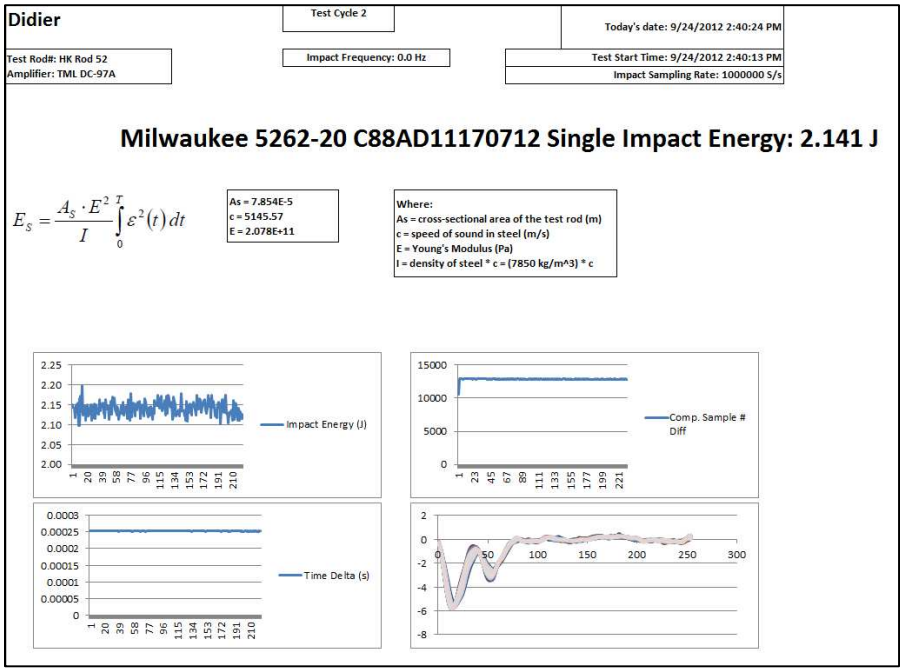

Figure 3-3: Typical test run report with no errors

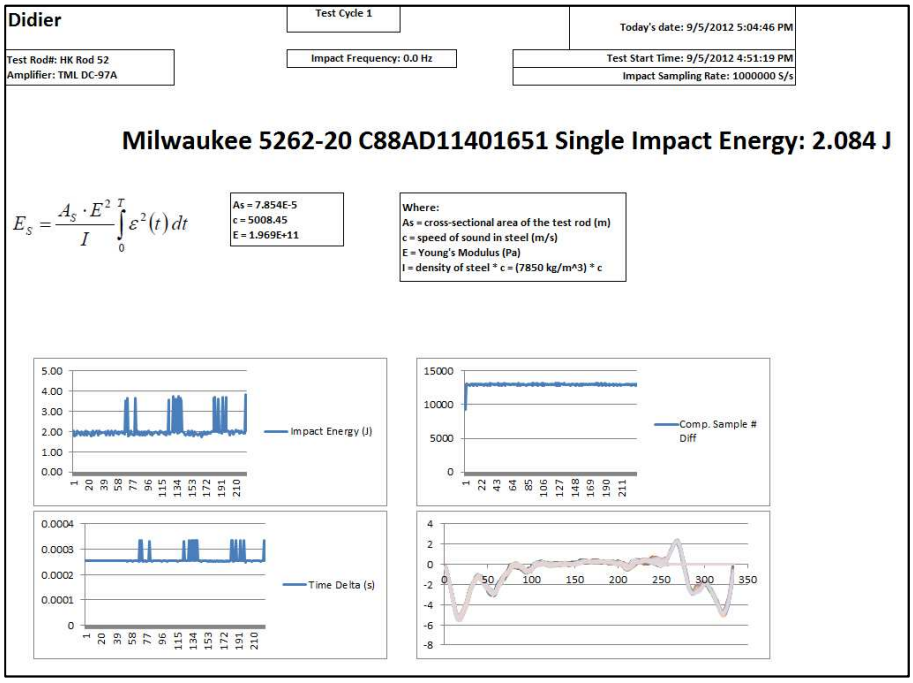

Figure 3-4: Test report containing errors in impact energy, time step, and strain signature data

The test procedure was repeated three times for each tool, as specified by ETPA 05/2009. At the completion of three test runs, the current draw of the tool in hammer-only mode while breaking concrete was measured with a multimeter applied to the tool's power cord. The impact energy and frequency for the tool was calculated as the average of the measured values from every test run for all seven samples. The averaged test results are listed in Table 4-2. Detailed results for each tool and test run can be found in Appendix C

Measurement	Value
Tool	Milwaukee 5262-20
Voltage [V]	120
Current, hammer only [A]	4.6
Feed Force [N]	120
Impact Frequency [Hz]	76.8
Impact Frequency [min^{-1}]	4608
Impact Energy [J]	2.15

Table 3-2: Average impact energy test results

4 Results, Discussion, Conclusions, and Future Recommendations

The performance data gathered during impact energy testing was compared to the corresponding outputs calculated by the mathematical model. The results can be seen side by side in Table 5-1.

Performance Parameter	Model Result	Test Result	%Δ
Impact energy [J]	2.34	2.15	8.84
Impact frequency [min^{-1}]	4372	4608	-5.12
Chisel-mode current draw [A]	5.78	4.60	25.65

Table 4-1: Comparison of model predicted performance to measured performance

The model results exhibited good agreement with the test data. Impact energy and impact frequency outputs from the model were within 10% of their measured values, while the chisel-mode current draw of the tool was about 1.0A lower than predicted. While the performance estimation generated by the mathematical model does not precisely match the measured performance of the tool, the level of accuracy obtained is more than adequate for development of new rotary hammers.

The validation of the model provides the rotary hammer designer with a powerful tool for synthesizing new designs that are able to approach the target performance on the first prototype iteration. The end result is the ability to compress new product development timelines and deliver a product that exceeds the expectations of the user. Not only is the model being actively employed in the creation of new rotary hammer

designs, but existing models of rotary hammers are being analyzed with the model to better understand their performance and further validate the capabilities of the model.

4.1 Potential Sources of Error

There are several possible sources of error that the difference between the model result and test data can be attributed to. These errors may lie in both the assumptions and formulation of the model as well as the test procedure used to validate it.

The mathematical model assumes that the portion of the striker's kinetic energy that is transferred into the anvil and bit is the tool's impact energy. In reality, a small portion of the transferred energy is lost to sound and internal heating of the anvil and bit due to elastic deformation of the anvil and bit as the impact stress wave travels along these components. Additionally, energy may be lost to sliding friction at the points of contact between the striker, anvil, bit, and concrete.

A number of assumptions were made to simplify the formulation of the model. The thermodynamic conditions inside the piston working chamber assume that the air column trapped inside the chamber behaves as an ideal gas. Due to the temperatures and pressures attained inside the chamber, the air column's behavior may depart significantly from the ideal model (9).

Further sources of error include manufacturing variances present in the tested tools and measurement error present in the test rods or DAQ equipment.

4.2 Other Applications

In addition to its primary function of performance prediction, secondary outputs calculated by the model can be used to aid in component design. The calculated pressure of the air in the piston working chamber can be used to assess the ability of the striker o-ring to effectively seal the working chamber without causing wear on the inside of the piston due to excessive compression. The force acting on the striker is used as a bearing reaction load for the purposes of determining bearing life. The torque and speeds calculated at the spindle, motor and intermediate shafts find use as inputs in design of gearing capable of transmitting power through the mechanism.

4.3 Improvements and Future Work

Although the mathematical model described in this study has been shown to provide a reasonably accurate prediction of rotary hammer performance, there are still opportunities to improve the function of the model and expand its capabilities. Additionally, the model has opened up the possibility to research ways to manipulate various aspects of rotary hammer designs to improve performance.

The model is currently based on a backward-difference numerical integration scheme, utilizing the Euler method and the Taylor series to compute component velocity and position at each time step. While this formulation was relatively easy to implement and attained reasonable results, it is not as accurate as other well-known numerical integration techniques. Furthermore, a small time step is required in order to

achieve the desired accuracy. For a model that requires a significant amount of time to reach steady state, a small time step can prove to be costly from a computational perspective. Investigation is ongoing into adapting the model to use the fourth-order Runge-Kutta integration scheme in an effort to improve the model's accuracy and reduce the computational expense (7).

The model's accuracy can be improved further with a more accurate treatment of the thermodynamics of the piston working chamber. Rather than using the ideal gas model, other equations of state, such as the Van der Waals or Redlich-Kwong equations, might be employed (12).

The functionality of the impact energy test fixture is currently in the process of being expanded to include the ability to record the pre- and post-impact velocities of the striker inside a rotary hammer to calculate striker kinetic energy alongside the impact energy measurement from the test rod, similar to the process used to validate the test fixture. This additional function will enable the measurement of the portion of striker kinetic energy that is not converted to impact energy and allow further improvement to the model by accounting for lost energy. This additional test procedure necessitates modification of the test tool by cutting a passage through the tool housing, spindle, and piston to allow the laser curtain to track striker displacement.

Recently, the model has been modified to include an optimization function. The optimization version of the model functions by allowing the input parameters to be set as optimization variables, each constrained to a particular range of values specified by

the designer. The optimization algorithm then repeatedly runs iterations of the model using random combinations of the input variables, staying within the specified range for each variable. The performance predictions are then plotted, allowing the designer to review the results for any combinations that may meet the desired performance targets. This method is effective at providing a number of candidate designs without the need for trial and error, but the computational effort required by the integration technique is magnified when the model is recalculated thousands of times for different input combinations. It is hoped that this issue will be mitigated by implementing a more efficient integration scheme as mentioned earlier.

In addition to developing the optimization version of the model, preliminary work is being carried out on integrating the optimization version with parallel work being done to correlate drill rate for a given bit size to performance characteristics such as impact energy, impacts per minute, and spindle revolutions per minute. The ultimate goal of this effort would be to optimize a rotary hammer design to perform well in key applications that represent the majority of the tool's use.

References

1. **DeWalt.** DeWalt Compact SDS Rotary Hammers. *DeWalt.* [Online] [Cited: November 19, 2012.] http://dewalt.com/tool-categories/hammerdrills--hammers-compact-sds-rotary-hammers.aspx.

2. **Makita U.S.A., Inc.** Rotary Hammers. *Makita.* [Online] [Cited: November 19, 2012.] http://makita.com/en-us/Modules/Tools/Default.aspx?CatID=45.

3. **Milwaukee Electric Tool Corporation.** SDS+ Rotary Hammers. *Milwaukee Tool.* [Online] [Cited: November 19, 2012.] http://www.milwaukeetool.com/tools/rotary-hammers-and-hammer-drills/hammers-rotary/sds-hammers.

4. **Robert Bosch GmbH.** Rotary Hammers. *Bosch Power Tools.* [Online] [Cited: November 19, 2012.] http://www.boschtools.com/Products/Tools/Pages/ItemResults.aspx?catid=1068.

5. **Milwaukee Electric Tool Corporation.** 5262-20 Operator's Manual. Brookfield : Milwaukee Electric Tool Corporation, 2011.

6. —. 7/8" SDS Plus Rotary Hammer Kit 5262-21. *Milwaukee Electric Tool.* [Online] [Cited: 11 12, 2012.] http://www.milwaukeetool.com/tools/rotary-hammers-and-hammer-drills/hammers-rotary/sds-hammers/7-8-inch-sds-plus-rotary-hammer-kit/5262-21.

7. **Chapra, Steven C. and Canale, P. Raymond.** *Numerical Methods for Engineers, 6th Ed.* New York : McGraw-Hill, 2010.

8. **Parker Hannifin Corporation.** Parker O-Ring Handbook. Cleveland : Parker Hannifin Corporation, 2007.

9. **Moran, Michael J. and Shapiro, Howard N.** *Fundamentals of Engineering Thermodynamics, 5th Ed.* s.l. : John Wiley & Sons, Ltd., 2006.

10. **European Power Tool Association.** Procedure 05/2009 - Measurment of the single impact energy of rotary hammers and breakers. Frankfurt : European Power Tool Association, 2009.

11. **Doyle, Scott.** *Impact Energy Testing - Trials and Triumphs.* Brookfield : Milwaukee Electric Tool Corporation, Internal Document, 2012.

12. **Engel, Thomas and Reid, Philip.** *Thermodynamics, Statistical Thermodynamics, & Kinetics, 2nd ed.* s.l. : Prentice Hall, 2009.

Appendix A: Test Rod Verification Results

The following data are detailed test reports generated during verification trial of the impact energy test rods. The data given are for both rods used during impact energy testing. The rod identification number is noted in the upper left corner of the report. The summarized test rod verification results were previously presented in Section 4.2.

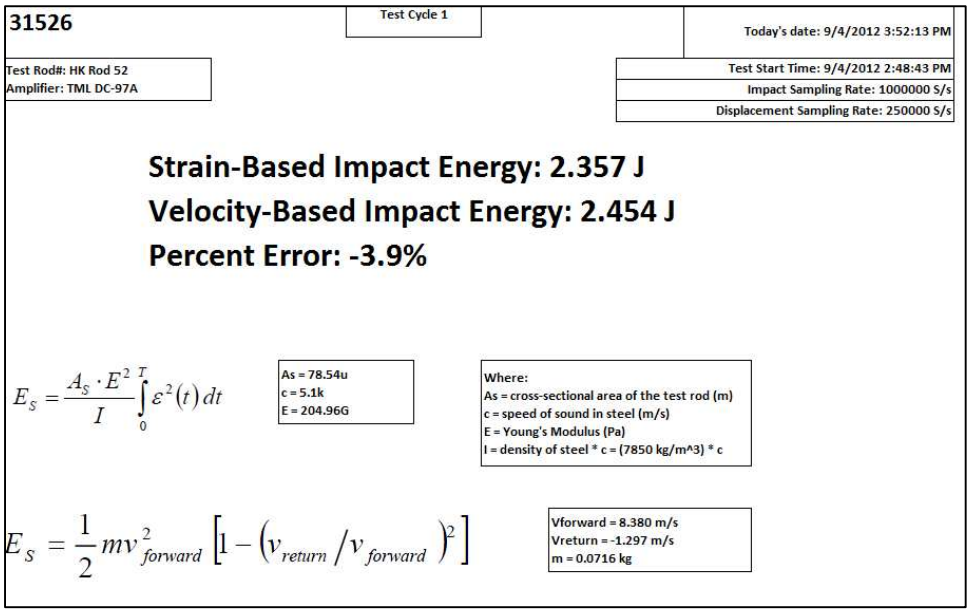

31526

Test Cycle 2

Today's date: 9/4/2012 3:57:17 PM

Test Rod#: HK Rod 52
Amplifier: TML DC-97A

Test Start Time: 9/4/2012 3:56:44 PM
Impact Sampling Rate: 1000000 S/s
Displacement Sampling Rate: 250000 S/s

Strain-Based Impact Energy: 2.333 J
Velocity-Based Impact Energy: 2.426 J
Percent Error: -3.9%

$$E_S = \frac{A_S \cdot E^2}{I} \int_0^T \varepsilon^2(t)\,dt$$

As = 78.54u
c = 5.1k
E = 204.96G

Where:
As = cross-sectional area of the test rod (m)
c = speed of sound in steel (m/s)
E = Young's Modulus (Pa)
I = density of steel * c = (7850 kg/m^3) * c

$$E_S = \frac{1}{2} m v_{forward}^2 \left[1 - \left(v_{return} / v_{forward}\right)^2\right]$$

Vforward = 8.330 m/s
Vreturn = -1.271 m/s
m = 0.0716 kg

31526

Test Cycle 3

Today's date: 9/4/2012 4:29:24 PM

Test Rod#: HK Rod 52
Amplifier: TML DC-97A

Test Start Time: 9/4/2012 4:28:47 PM
Impact Sampling Rate: 1000000 S/s
Displacement Sampling Rate: 250000 S/s

Strain-Based Impact Energy: 2.419 J
Velocity-Based Impact Energy: 2.490 J
Percent Error: -2.9%

$$E_S = \frac{A_S \cdot E^2}{I} \int_0^T \varepsilon^2(t)\,dt$$

As = 78.54u
c = 5.1k
E = 204.96G

Where:
As = cross-sectional area of the test rod (m)
c = speed of sound in steel (m/s)
E = Young's Modulus (Pa)
I = density of steel * c = (7850 kg/m^3) * c

$$E_S = \frac{1}{2} m v_{forward}^2 \left[1 - \left(v_{return} / v_{forward}\right)^2\right]$$

Vforward = 8.429 m/s
Vreturn = -1.230 m/s
m = 0.0716 kg

31526

Test Cycle 4

Today's date: 9/4/2012 4:33:41 PM

Test Rod#: HK Rod 52
Amplifier: TML DC-97A

Test Start Time: 9/4/2012 4:33:13 PM
Impact Sampling Rate: 1000000 S/s
Displacement Sampling Rate: 250000 S/s

Strain-Based Impact Energy: 2.465 J
Velocity-Based Impact Energy: 2.516 J
Percent Error: -2.0%

$$E_S = \frac{A_S \cdot E^2}{I} \int_0^T \varepsilon^2(t)\,dt$$

As = 78.54u
c = 5.1k
E = 204.96G

Where:
As = cross-sectional area of the test rod (m)
c = speed of sound in steel (m/s)
E = Young's Modulus (Pa)
I = density of steel * c = (7850 kg/m^3) * c

$$E_S = \frac{1}{2} m v_{forward}^2 \left[1 - \left(v_{return} / v_{forward}\right)^2\right]$$

Vforward = 8.472 m/s
Vreturn = -1.223 m/s
m = 0.0716 kg

31526

Test Cycle 5

Today's date: 9/4/2012 4:35:30 PM

Test Rod#: HK Rod 52
Amplifier: TML DC-97A

Test Start Time: 9/4/2012 4:35:02 PM
Impact Sampling Rate: 1000000 S/s
Displacement Sampling Rate: 250000 S/s

Strain-Based Impact Energy: 2.411 J
Velocity-Based Impact Energy: 2.474 J
Percent Error: -2.5%

$$E_S = \frac{A_S \cdot E^2}{I} \int_0^T \varepsilon^2(t)\,dt$$

As = 78.54u
c = 5.1k
E = 204.96G

Where:
As = cross-sectional area of the test rod (m)
c = speed of sound in steel (m/s)
E = Young's Modulus (Pa)
I = density of steel * c = (7850 kg/m^3) * c

$$E_S = \frac{1}{2} m v_{forward}^2 \left[1 - \left(v_{return} / v_{forward}\right)^2\right]$$

Vforward = 8.411 m/s
Vreturn = -1.282 m/s
m = 0.0716 kg

Komas

Test Cycle 1

Today's date: 9/28/2012 2:05:01 PM

Test Rod#: HK Rod 55
Amplifier: TML DC-97A

Test Start Time: 9/28/2012 2:04:41 PM
Impact Sampling Rate: 1000000 S/s
Displacement Sampling Rate: 250000 S/s

Strain-Based Impact Energy: 2.355 J
Velocity-Based Impact Energy: 2.377 J
Percent Error: -0.9%

$$E_S = \frac{A_S \cdot E^2}{I} \int_0^T \varepsilon^2(t)\,dt$$

As = 78.54u
c = 5.1k
E = 204.96G

Where:
As = cross-sectional area of the test rod (m)
c = speed of sound in steel (m/s)
E = Young's Modulus (Pa)
I = density of steel * c = (7850 kg/m^3) * c

$$E_S = \frac{1}{2} m v_{forward}^2 \left[1 - \left(v_{return} / v_{forward}\right)^2\right]$$

Vforward = 8.249 m/s
Vreturn = -1.282 m/s
m = 0.0716 kg

Komas

Test Cycle 2

Today's date: 9/28/2012 2:05:49 PM

Test Rod#: HK Rod 55
Amplifier: TML DC-97A

Test Start Time: 9/28/2012 2:05:35 PM
Impact Sampling Rate: 1000000 S/s
Displacement Sampling Rate: 250000 S/s

Strain-Based Impact Energy: 2.356 J
Velocity-Based Impact Energy: 2.345 J
Percent Error: 0.5%

$$E_S = \frac{A_S \cdot E^2}{I} \int_0^T \varepsilon^2(t)\,dt$$

As = 78.54u
c = 5.1k
E = 204.96G

Where:
As = cross-sectional area of the test rod (m)
c = speed of sound in steel (m/s)
E = Young's Modulus (Pa)
I = density of steel * c = (7850 kg/m^3) * c

$$E_S = \frac{1}{2} m v_{forward}^2 \left[1 - \left(v_{return} / v_{forward}\right)^2\right]$$

Vforward = 8.193 m/s
Vreturn = -1.280 m/s
m = 0.0716 kg

Komas

Test Cycle 3

Today's date: 9/28/2012 2:06:30 PM

Test Rod#: HK Rod 55
Amplifier: TML DC-97A

Test Start Time: 9/28/2012 2:06:16 PM
Impact Sampling Rate: 1000000 S/s
Displacement Sampling Rate: 250000 S/s

Strain-Based Impact Energy: 2.340 J
Velocity-Based Impact Energy: 2.335 J
Percent Error: 0.2%

$$E_S = \frac{A_S \cdot E^2}{I} \int_0^T \varepsilon^2(t)\,dt$$

As = 78.54u
c = 5.1k
E = 204.96G

Where:
As = cross-sectional area of the test rod (m)
c = speed of sound in steel (m/s)
E = Young's Modulus (Pa)
I = density of steel * c = (7850 kg/m^3) * c

$$E_S = \frac{1}{2} m v_{forward}^2 \left[1 - \left(v_{return} / v_{forward}\right)^2\right]$$

Vforward = 8.183 m/s
Vreturn = -1.317 m/s
m = 0.0716 kg

Komas

Test Cycle 4

Today's date: 9/28/2012 2:07:17 PM

Test Rod#: HK Rod 55
Amplifier: TML DC-97A

Test Start Time: 9/28/2012 2:06:55 PM
Impact Sampling Rate: 1000000 S/s
Displacement Sampling Rate: 250000 S/s

Strain-Based Impact Energy: 2.315 J
Velocity-Based Impact Energy: 2.314 J
Percent Error: 0.0%

$$E_S = \frac{A_S \cdot E^2}{I} \int_0^T \varepsilon^2(t)\,dt$$

As = 78.54u
c = 5.1k
E = 204.96G

Where:
As = cross-sectional area of the test rod (m)
c = speed of sound in steel (m/s)
E = Young's Modulus (Pa)
I = density of steel * c = (7850 kg/m^3) * c

$$E_S = \frac{1}{2} m v_{forward}^2 \left[1 - \left(v_{return} / v_{forward}\right)^2\right]$$

Vforward = 8.123 m/s
Vreturn = -1.153 m/s
m = 0.0716 kg

Komas

Test Cycle 5

Today's date: 9/28/2012 2:08:14 PM

Test Rod#: HK Rod 55
Amplifier: TML DC-97A

Test Start Time: 9/28/2012 2:08:02 PM
Impact Sampling Rate: 1000000 S/s
Displacement Sampling Rate: 250000 S/s

Strain-Based Impact Energy: 2.398 J
Velocity-Based Impact Energy: 2.358 J
Percent Error: 1.7%

$$E_S = \frac{A_S \cdot E^2}{I} \int_0^T \varepsilon^2(t)\,dt$$

As = 78.54u
c = 5.1k
E = 204.96G

Where:
As = cross-sectional area of the test rod (m)
c = speed of sound in steel (m/s)
E = Young's Modulus (Pa)
I = density of steel * c = (7850 kg/m^3) * c

$$E_S = \frac{1}{2} m v_{forward}^2 \left[1 - \left(v_{return} / v_{forward}\right)^2\right]$$

Vforward = 8.206 m/s
Vreturn = -1.217 m/s
m = 0.0716 kg

Appendix B: Impact Energy Test Results

The data presented in this appendix are the summarized testing results for each test subject. Following the summarized results are detailed test reports for every test trial conducted for each tool, including plots of the test rod strain signature, impact energy for each impact during the trial, and the impact duration for each impact. The averaged result for all tools and all test trials was previously given in Section 4.3.

Sample #	Make	Model	S/N	Date of Measurement	Feed Force [N]	Voltage [V]	Current [A]	Impact Frequency [Hz]	Impact Energy [J]	Avg Impact Frequency [Hz]	Avg. Impact Energy [J]	Test Rod
								76.2	1.97			
								75.8	1.97			
1	Milwaukee	5262-20	C88AD114201695	5-Sep-12	120	120	4.7	76	1.94	76	1.96	HK52
								76	2.08			
								77.1	2.12			
2	Milwaukee	5262-20	C88AD114201651	21-Sep-12	120	120	4.6	77.1	2.12	76.73333333	2.106666667	HK52
								76.2	2.28			
								77.3	2.26			
3	Milwaukee	5262-20	C88AD114201693	21-Sep-12	120	120	4.4	77.3	2.24	76.93333333	2.26	HK52
								77	2.17			
								77	2.18			
4	Milwaukee	5262-20	C88AD11170744	25-Sep-12	120	120	4.7	77.2	2.25	77.06666667	2.2	HK52
								77.2	2.1			
								77.6	2.14			
5	Milwaukee	5262-20	C88AD11170712	25-Sep-12	120	120	4.6	77.5	2.13	77.43333333	2.123333333	HK52
								76.8	2.28			
								76.7	2.15			
6	Milwaukee	5262-20	C88AD114201652	2-Oct-12	120	120	4.5	76.9	2.16	76.76666667	2.21	HK55
								76.8	2.18			
								76.8	2.17			
7	Milwaukee	5262-20	C88AD114200282	2-Oct-12	120	120	4.5	77	2.27	76.86666667	2.206666667	HK55

Didier

Test Cycle 1

Today's date: 9/5/2012 4:36:59 PM

Test Rod#: HK Rod 52
Amplifier: TML DC-97A

Impact Frequency: 0.0 Hz

Test Start Time: 9/5/2012 4:36:12 PM
Impact Sampling Rate: 1000000 S/s

Milwaukee 5262-20 C88AD11401635 Single Impact Energy: 1.969 J

$$E_S = \frac{A_S \cdot E^2}{I} \int_0^T \varepsilon^2(t)\,dt$$

As = 7.854E-5
c = 5152.07
E = 2.084E+11

Where:
As = cross-sectional area of the test rod (m)
c = speed of sound in steel (m/s)
E = Young's Modulus (Pa)
I = density of steel * c = (7850 kg/m^3) * c

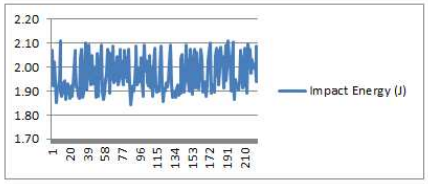

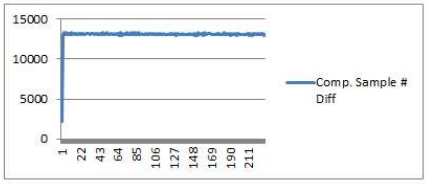

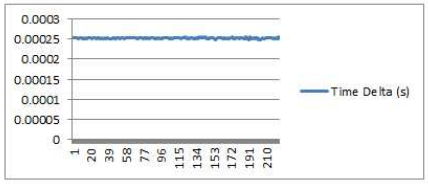

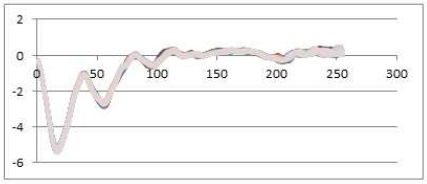

Didier

Test Cycle 2

Today's date: 9/5/2012 4:37:50 PM

Test Rod#: HK Rod 52
Amplifier: TML DC-97A

Impact Frequency: 0.0 Hz

Test Start Time: 9/5/2012 4:37:31 PM
Impact Sampling Rate: 1000000 S/s

Milwaukee 5262-20 C88AD11401635 Single Impact Energy: 1.966 J

$$E_S = \frac{A_S \cdot E^2}{I} \int_0^T \varepsilon^2(t)\,dt$$

As = 7.854E-5
c = 5154.15
E = 2.085E+11

Where:
As = cross-sectional area of the test rod (m)
c = speed of sound in steel (m/s)
E = Young's Modulus (Pa)
I = density of steel * c = (7850 kg/m^3) * c

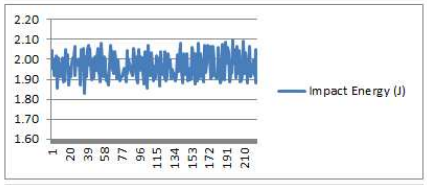

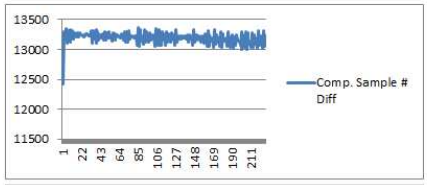

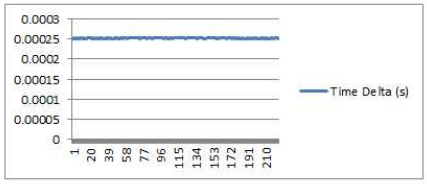

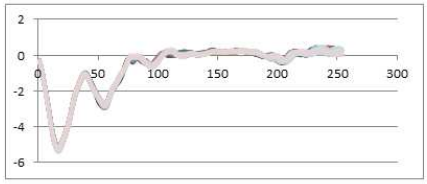

Didier

Test Cycle 3

Today's date: 9/5/2012 4:38:29 PM

Test Rod#: HK Rod 52
Amplifier: TML DC-97A

Impact Frequency: 0.0 Hz

Test Start Time: 9/5/2012 4:38:16 PM
Impact Sampling Rate: 1000000 S/s

Milwaukee 5262-20 C88AD11401635 Single Impact Energy: 1.942 J

$$E_S = \frac{A_S \cdot E^2}{I} \int_0^T \varepsilon^2(t)\,dt$$

As = 7.854E-5
c = 4713.75
E = 1.744E+11

Where:
As = cross-sectional area of the test rod (m)
c = speed of sound in steel (m/s)
E = Young's Modulus (Pa)
I = density of steel * c = (7850 kg/m^3) * c

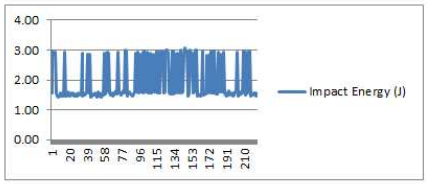

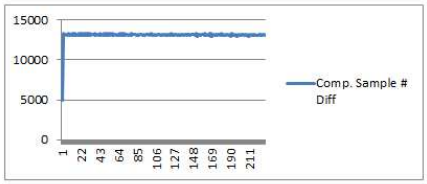

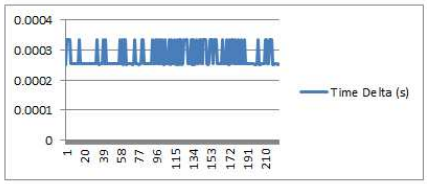

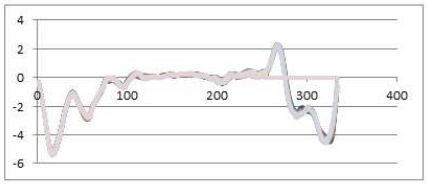

Didier

Test Cycle 1

Today's date: 9/5/2012 5:04:46 PM

Test Rod#: HK Rod 52
Amplifier: TML DC-97A

Impact Frequency: 0.0 Hz

Test Start Time: 9/5/2012 4:51:19 PM
Impact Sampling Rate: 1000000 S/s

Milwaukee 5262-20 C88AD11401651 Single Impact Energy: 2.084 J

$$E_S = \frac{A_S \cdot E^2}{I} \int_0^T \varepsilon^2(t)\,dt$$

As = 7.854E-5
c = 5008.45
E = 1.969E+11

Where:
As = cross-sectional area of the test rod (m)
c = speed of sound in steel (m/s)
E = Young's Modulus (Pa)
I = density of steel * c = (7850 kg/m^3) * c

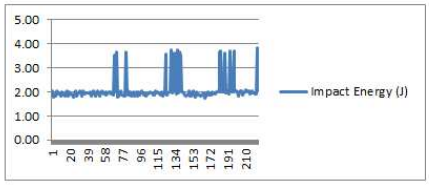

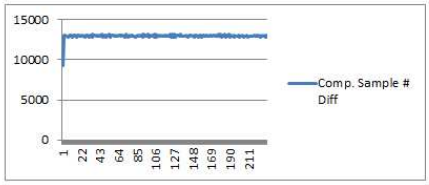

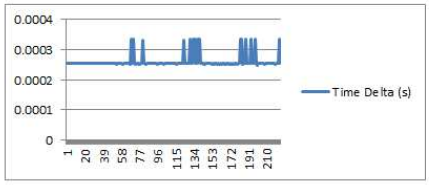

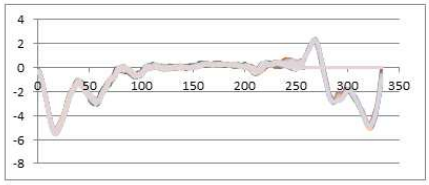

Didier

Test Cycle 2

Today's date: 9/21/2012 12:38:01 PM

Test Rod#: HK Rod 52
Amplifier: TML DC-97A

Impact Frequency: 0.0 Hz

Test Start Time: 9/21/2012 12:37:40 PM
Impact Sampling Rate: 1000000 S/s

Milwaukee 5262-20 C88AD11401651 Single Impact Energy: 2.115 J

$$E_S = \frac{A_S \cdot E^2}{I} \int_0^T \varepsilon^2(t)\,dt$$

As = 7.854E-5
c = 5144.21
E = 2.077E+11

Where:
As = cross-sectional area of the test rod (m)
c = speed of sound in steel (m/s)
E = Young's Modulus (Pa)
I = density of steel * c = (7850 kg/m^3) * c

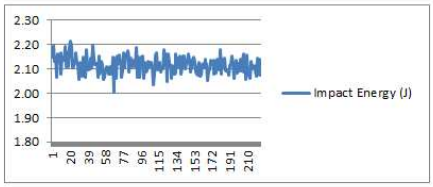

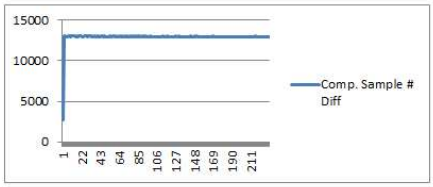

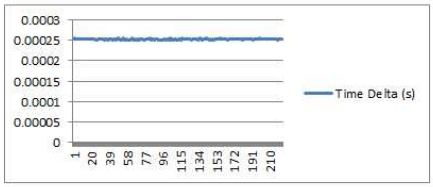

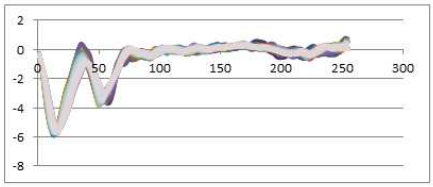

Didier

Test Cycle 3

Today's date: 9/21/2012 12:42:05 PM

Test Rod#: HK Rod 52
Amplifier: TML DC-97A

Impact Frequency: 0.0 Hz

Test Start Time: 9/21/2012 12:41:54 PM
Impact Sampling Rate: 1000000 S/s

Milwaukee 5262-20 C88AD11401651 Single Impact Energy: 2.119 J

$$E_S = \frac{A_S \cdot E^2}{I} \int_0^T \varepsilon^2(t)\,dt$$

As = 7.854E-5
c = 5130.70
E = 2.066E+11

Where:
As = cross-sectional area of the test rod (m)
c = speed of sound in steel (m/s)
E = Young's Modulus (Pa)
I = density of steel * c = (7850 kg/m^3) * c

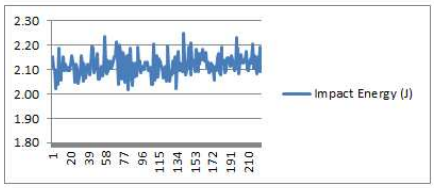

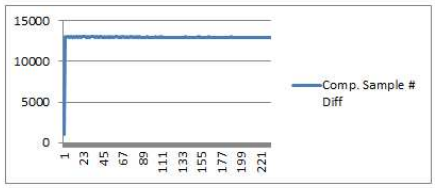

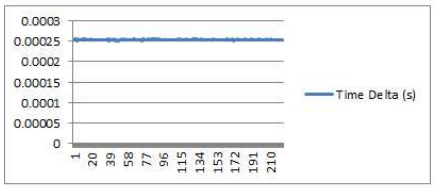

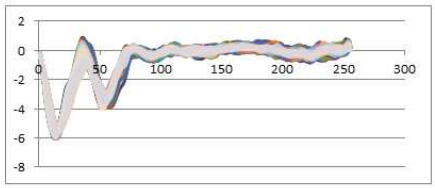

Didier

Test Cycle 1

Today's date: 9/21/2012 12:52:51 PM

Test Rod#: HK Rod 52
Amplifier: TML DC-97A

Impact Frequency: 0.0 Hz

Test Start Time: 9/21/2012 12:52:26 PM
Impact Sampling Rate: 1000000 S/s

Milwaukee 5262-20 C88AD11401653 Single Impact Energy: 2.282 J

$$E_S = \frac{A_S \cdot E^2}{I} \int_0^T \varepsilon^2(t)\,dt$$

As = 7.854E-5
c = 5138.88
E = 2.073E+11

Where:
As = cross-sectional area of the test rod (m)
c = speed of sound in steel (m/s)
E = Young's Modulus (Pa)
I = density of steel * c = (7850 kg/m^3) * c

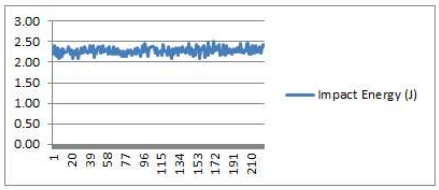

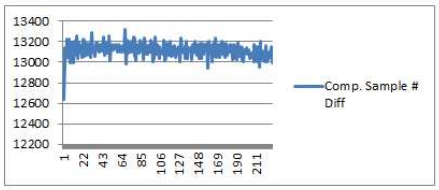

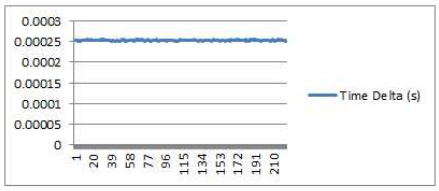

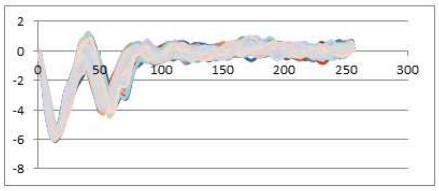

Didier

Test Cycle 2

Today's date: 9/21/2012 12:57:12 PM

Test Rod#: HK Rod 52
Amplifier: TML DC-97A

Impact Frequency: 0.0 Hz

Test Start Time: 9/21/2012 12:57:01 PM
Impact Sampling Rate: 1000000 S/s

Milwaukee 5262-20 C88AD11401653 Single Impact Energy: 2.239 J

$$E_S = \frac{A_S \cdot E^2}{I} \int_0^T \varepsilon^2(t)\,dt$$

As = 7.854E-5
c = 5138.82
E = 2.073E+11

Where:
As = cross-sectional area of the test rod (m)
c = speed of sound in steel (m/s)
E = Young's Modulus (Pa)
I = density of steel * c = (7850 kg/m^3) * c

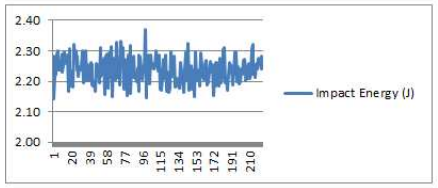

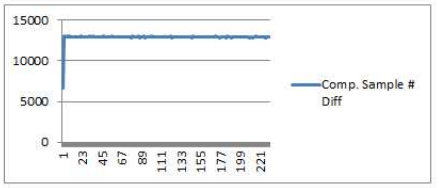

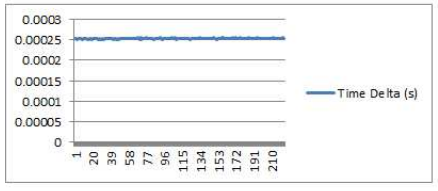

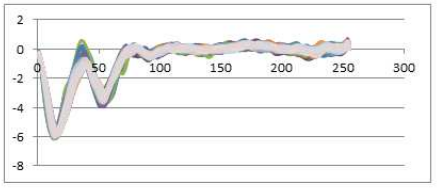

Didier

Test Cycle 3

Today's date: 9/21/2012 12:55:18 PM

Test Rod#: HK Rod 52
Amplifier: TML DC-97A

Impact Frequency: 0.0 Hz

Test Start Time: 9/21/2012 12:55:06 PM
Impact Sampling Rate: 1000000 S/s

Milwaukee 5262-20 C88AD11401653 Single Impact Energy: 2.256 J

$$E_S = \frac{A_S \cdot E^2}{I} \int_0^T \varepsilon^2(t)\,dt$$

As = 7.854E-5
c = 5145.99
E = 2.079E+11

Where:
As = cross-sectional area of the test rod (m)
c = speed of sound in steel (m/s)
E = Young's Modulus (Pa)
I = density of steel * c = (7850 kg/m^3) * c

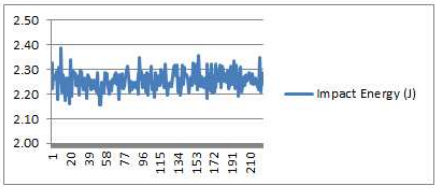

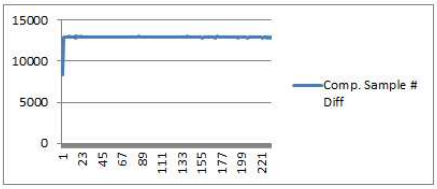

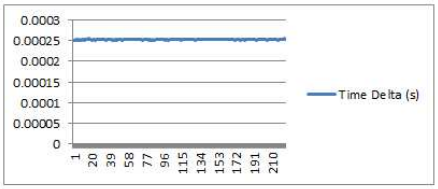

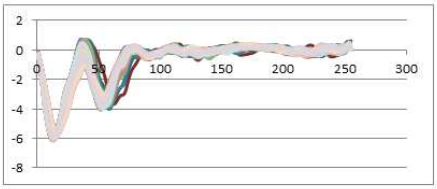

Didier

Test Cycle 1

Today's date: 9/24/2012 2:20:30 PM

Test Rod#: HK Rod 52
Amplifier: TML DC-97A

Impact Frequency: 0.0 Hz

Test Start Time: 9/24/2012 2:20:16 PM
Impact Sampling Rate: 1000000 S/s

Milwaukee 5262-20 C88AD11170744 Single Impact Energy: 2.171 J

$$E_S = \frac{A_S \cdot E^2}{I} \int_0^T \varepsilon^2(t)\,dt$$

As = 7.854E-5
c = 5148.70
E = 2.081E+11

Where:
As = cross-sectional area of the test rod (m)
c = speed of sound in steel (m/s)
E = Young's Modulus (Pa)
I = density of steel * c = (7850 kg/m^3) * c

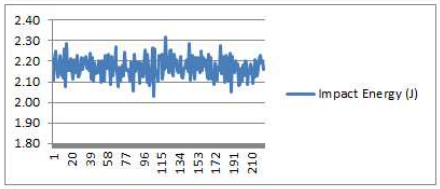

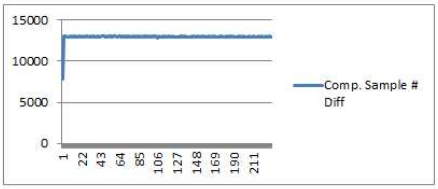

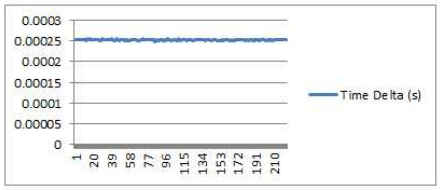

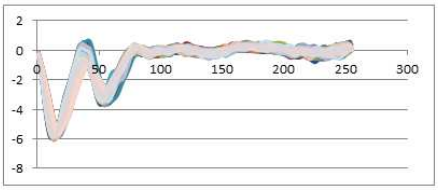

Didier

Test Cycle 2

Today's date: 9/24/2012 2:23:37 PM

Test Rod#: HK Rod 52
Amplifier: TML DC-97A

Impact Frequency: 0.0 Hz

Test Start Time: 9/24/2012 2:22:57 PM
Impact Sampling Rate: 1000000 S/s

Milwaukee 5262-20 C88AD11170744 Single Impact Energy: 2.177 J

$$E_S = \frac{A_S \cdot E^2}{I} \int_0^T \varepsilon^2(t)\,dt$$

As = 7.854E-5
c = 5142.35
E = 2.076E+11

Where:
As = cross-sectional area of the test rod (m)
c = speed of sound in steel (m/s)
E = Young's Modulus (Pa)
I = density of steel * c = (7850 kg/m^3) * c

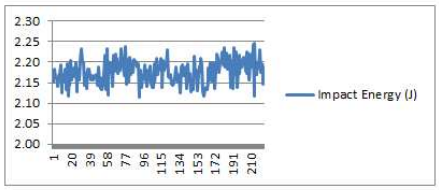

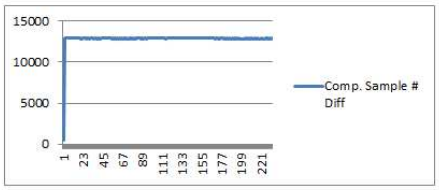

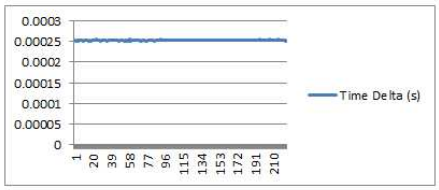

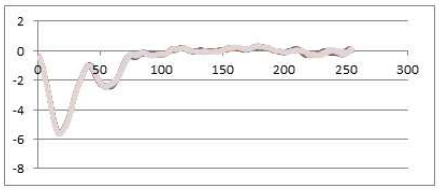

Didier

Test Cycle 3

Today's date: 9/24/2012 2:25:51 PM

Test Rod#: HK Rod 52
Amplifier: TML DC-97A

Impact Frequency: 0.0 Hz

Test Start Time: 9/24/2012 2:25:26 PM
Impact Sampling Rate: 1000000 S/s

Milwaukee 5262-20 C88AD11170744 Single Impact Energy: 2.251 J

$$E_S = \frac{A_S \cdot E^2}{I} \int_0^T \varepsilon^2(t)\,dt$$

As = 7.854E-5
c = 5172.85
E = 2.101E+11

Where:
As = cross-sectional area of the test rod (m)
c = speed of sound in steel (m/s)
E = Young's Modulus (Pa)
I = density of steel * c = (7850 kg/m^3) * c

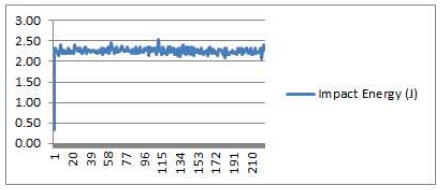

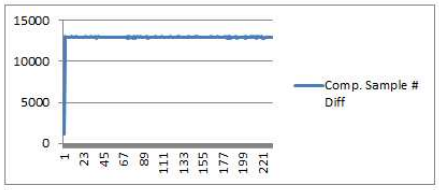

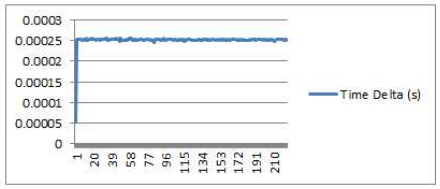

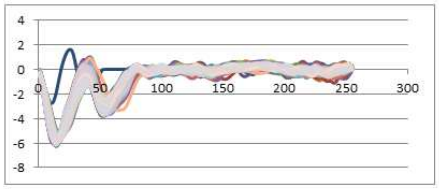

Didier

Test Cycle 1

Today's date: 9/24/2012 2:38:46 PM

Test Rod#: HK Rod 52
Amplifier: TML DC-97A

Impact Frequency: 0.0 Hz

Test Start Time: 9/24/2012 2:38:27 PM
Impact Sampling Rate: 1000000 S/s

Milwaukee 5262-20 C88AD11170712 Single Impact Energy: 2.103 J

$$E_S = \frac{A_S \cdot E^2}{I} \int_0^T \varepsilon^2(t)\,dt$$

As = 7.854E-5
c = 5124.36
E = 2.061E+11

Where:
As = cross-sectional area of the test rod (m)
c = speed of sound in steel (m/s)
E = Young's Modulus (Pa)
I = density of steel * c = (7850 kg/m^3) * c

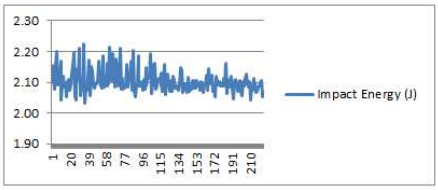

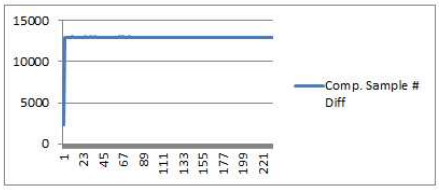

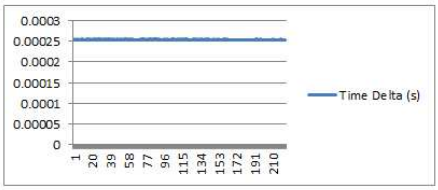

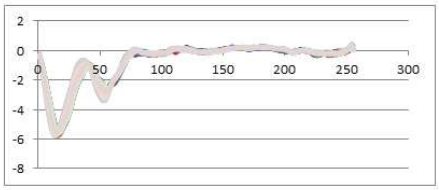

Didier

Test Cycle 2

Today's date: 9/24/2012 2:40:24 PM

Test Rod#: HK Rod 52
Amplifier: TML DC-97A

Impact Frequency: 0.0 Hz

Test Start Time: 9/24/2012 2:40:13 PM
Impact Sampling Rate: 1000000 S/s

Milwaukee 5262-20 C88AD11170712 Single Impact Energy: 2.141 J

$$E_S = \frac{A_S \cdot E^2}{I} \int_0^T \varepsilon^2(t)\,dt$$

As = 7.854E-5
c = 5145.57
E = 2.078E+11

Where:
As = cross-sectional area of the test rod (m)
c = speed of sound in steel (m/s)
E = Young's Modulus (Pa)
I = density of steel * c = (7850 kg/m^3) * c

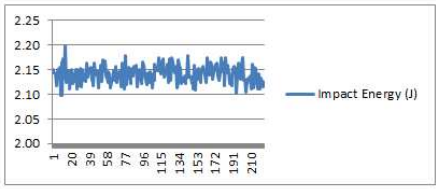

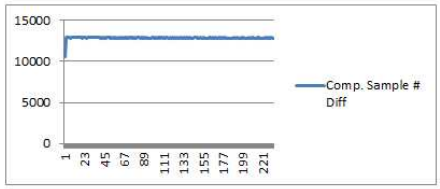

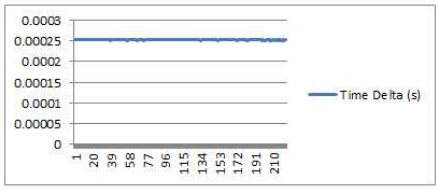

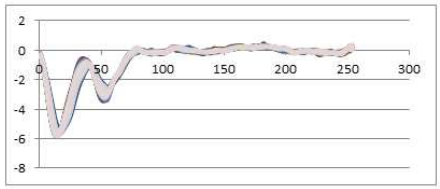

Didier

Test Cycle 3

Today's date: 9/24/2012 2:41:43 PM

Test Rod#: HK Rod 52
Amplifier: TML DC-97A

Impact Frequency: 0.0 Hz

Test Start Time: 9/24/2012 2:41:30 PM
Impact Sampling Rate: 1000000 S/s

Milwaukee 5262-20 C88AD11170712 Single Impact Energy: 2.130 J

$$E_S = \frac{A_S \cdot E^2}{I} \int_0^T \varepsilon^2(t)\,dt$$

As = 7.854E-5
c = 5140.13
E = 2.074E+11

Where:
As = cross-sectional area of the test rod (m)
c = speed of sound in steel (m/s)
E = Young's Modulus (Pa)
I = density of steel * c = (7850 kg/m^3) * c

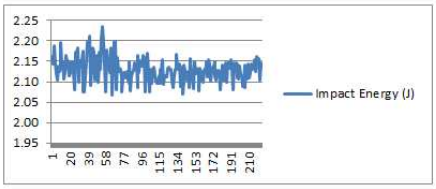

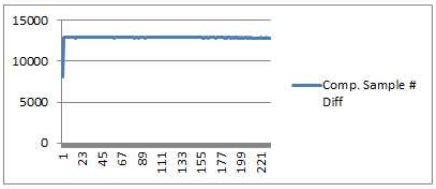

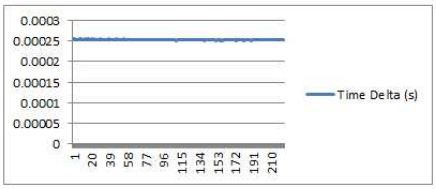

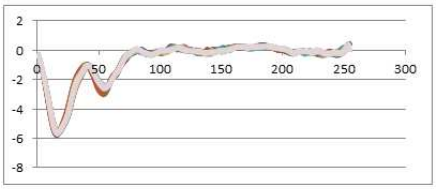

Didier

Test Cycle 1

Today's date: 10/2/2012 3:28:19 PM

Test Rod#: HK Rod 55
Amplifier: TML DC-97A

Impact Frequency: 0.0 Hz

Test Start Time: 10/2/2012 3:28:06 PM
Impact Sampling Rate: 1000000 S/s

Milwaukee 5262-20 CA88AD11401652 Single Impact Energy: 2.275 J

$$E_S = \frac{A_S \cdot E^2}{I} \int_0^T \varepsilon^2(t)\,dt$$

As = 7.854E-5
c = 5139.16
E = 2.073E+11

Where:
As = cross-sectional area of the test rod (m)
c = speed of sound in steel (m/s)
E = Young's Modulus (Pa)
I = density of steel * c = (7850 kg/m^3) * c

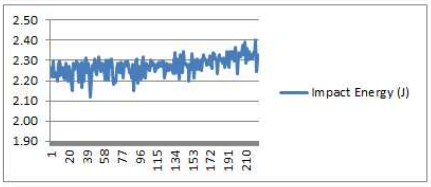

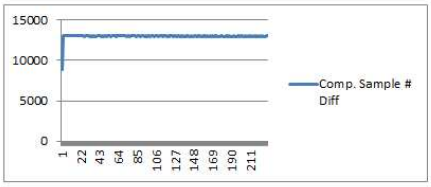

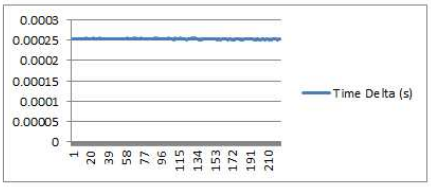

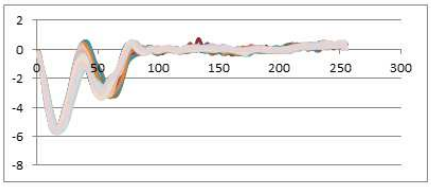

Didier

Test Cycle 3

Today's date: 10/2/2012 3:32:57 PM

Test Rod#: HK Rod 55
Amplifier: TML DC-97A

Impact Frequency: 0.0 Hz

Test Start Time: 10/2/2012 3:32:43 PM
Impact Sampling Rate: 1000000 S/s

Milwaukee 5262-20 CA88AD11401652 Single Impact Energy: 2.190 J

$$E_S = \frac{A_S \cdot E^2}{I} \int_0^T \varepsilon^2(t)\,dt$$

As = 7.854E-5
c = 5124.92
E = 2.062E+11

Where:
As = cross-sectional area of the test rod (m)
c = speed of sound in steel (m/s)
E = Young's Modulus (Pa)
I = density of steel * c = (7850 kg/m^3) * c

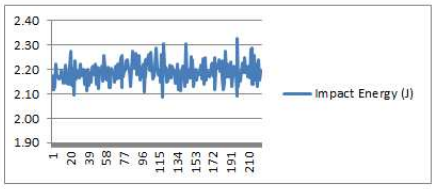

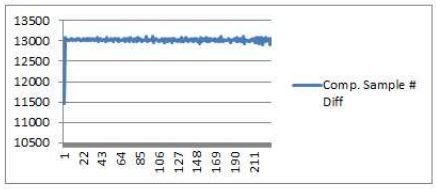

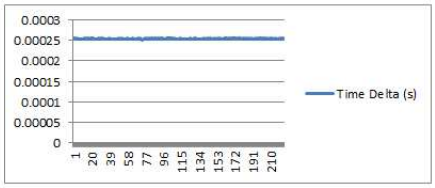

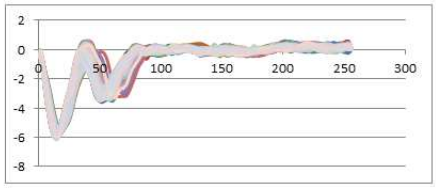

Didier

Test Cycle 4

Today's date: 10/2/2012 3:34:24 PM

Test Rod#: HK Rod 55
Amplifier: TML DC-97A

Impact Frequency: 0.0 Hz

Test Start Time: 10/2/2012 3:34:11 PM
Impact Sampling Rate: 1000000 S/s

Milwaukee 5262-20 CA88AD11401652 Single Impact Energy: 2.158 J

$$E_S = \frac{A_S \cdot E^2}{I} \int_0^T \varepsilon^2(t)\,dt$$

As = 7.854E-5
c = 5128.09
E = 2.064E+11

Where:
As = cross-sectional area of the test rod (m)
c = speed of sound in steel (m/s)
E = Young's Modulus (Pa)
I = density of steel * c = (7850 kg/m^3) * c

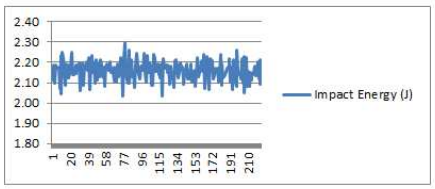

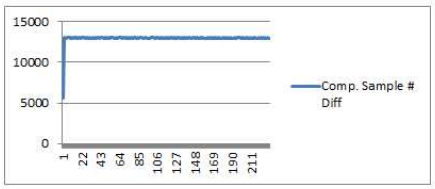

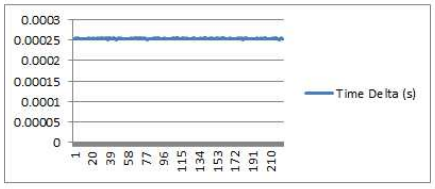

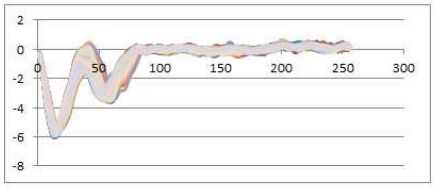

Didier

Test Cycle 1

Today's date: 10/2/2012 3:46:47 PM

Test Rod#: HK Rod 55
Amplifier: TML DC-97A

Impact Frequency: 0.0 Hz

Test Start Time: 10/2/2012 3:46:34 PM
Impact Sampling Rate: 1000000 S/s

Milwaukee 5262-20 CA88AD11400082 Single Impact Energy: 2.179 J

$$E_S = \frac{A_S \cdot E^2}{I} \int_0^T \varepsilon^2(t)\,dt$$

As = 7.854E-5
c = 5114.77
E = 2.054E+11

Where:
As = cross-sectional area of the test rod (m)
c = speed of sound in steel (m/s)
E = Young's Modulus (Pa)
I = density of steel * c = (7850 kg/m^3) * c

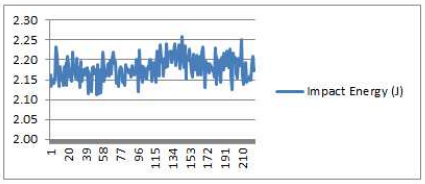

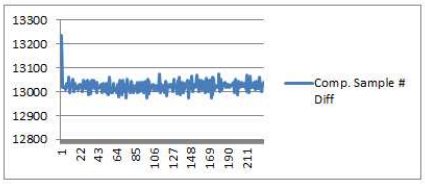

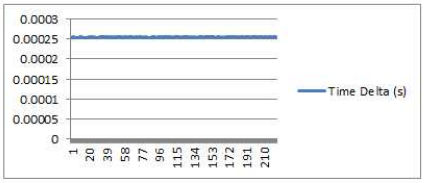

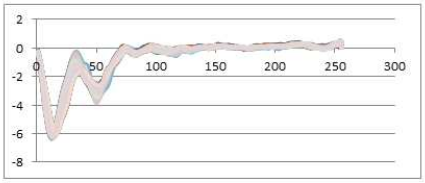

Didier

Test Cycle 2

Today's date: 10/2/2012 3:48:14 PM

Test Rod#: HK Rod 55
Amplifier: TML DC-97A

Impact Frequency: 0.0 Hz

Test Start Time: 10/2/2012 3:48:01 PM
Impact Sampling Rate: 1000000 S/s

Milwaukee 5262-20 CA88AD11400082 Single Impact Energy: 2.170 J

$$E_S = \frac{A_S \cdot E^2}{I} \int_0^T \varepsilon^2(t)\,dt$$

As = 7.854E-5
c = 5113.36
E = 2.052E+11

Where:
As = cross-sectional area of the test rod (m)
c = speed of sound in steel (m/s)
E = Young's Modulus (Pa)
I = density of steel * c = (7850 kg/m^3) * c

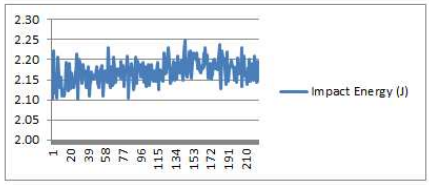

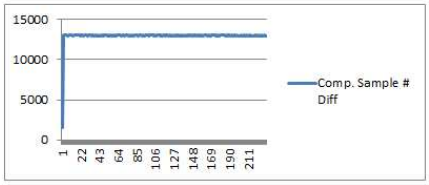

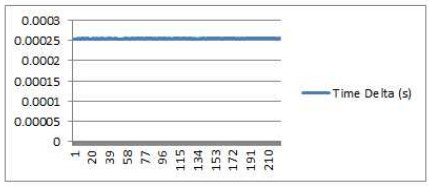

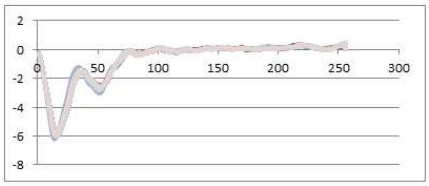

Didier

Test Cycle 3

Today's date: 10/2/2012 3:49:24 PM

Test Rod#: HK Rod 55
Amplifier: TML DC-97A

Impact Frequency: 0.0 Hz

Test Start Time: 10/2/2012 3:49:12 PM
Impact Sampling Rate: 1000000 S/s

Milwaukee 5262-20 CA88AD11400082 Single Impact Energy: 2.275 J

$$E_S = \frac{A_S \cdot E^2}{I} \int_0^T \varepsilon^2(t)\,dt$$

As = 7.854E-5
c = 5127.73
E = 2.064E+11

Where:
As = cross-sectional area of the test rod (m)
c = speed of sound in steel (m/s)
E = Young's Modulus (Pa)
I = density of steel * c = (7850 kg/m^3) * c